



PAPER • OPEN ACCESS

Bone on-a-chip: a 3D dendritic network in a screening platform for osteocyte-targeted drugs

To cite this article: Maria Veronica Lipreri *et al* 2023 *Biofabrication* **15** 045019

View the [article online](#) for updates and enhancements.

You may also like

- [In vitro model to study confined osteocyte networks exposed to flow-induced mechanical stimuli](#)
Kairui Zhang, Courtney Ogando, Alex Filip et al.
- [Biofabrication of vasculature in microphysiological models of bone](#)
Ian T Whelan, E Moeendarbary, David A Hoey et al.
- [Effect of external mechanical stimuli on human bone: a narrative review](#)
Megan E Mancuso, Andrew R Wilzman, Kyle E Murdock et al.

Biofabrication



PAPER

OPEN ACCESS

RECEIVED
13 January 2023

REVISED
2 August 2023

ACCEPTED FOR PUBLICATION
8 August 2023

PUBLISHED
1 September 2023

Original content from this work may be used under the terms of the [Creative Commons Attribution 4.0 licence](https://creativecommons.org/licenses/by/4.0/).

Any further distribution of this work must maintain attribution to the author(s) and the title of the work, journal citation and DOI.



Bone on-a-chip: a 3D dendritic network in a screening platform for osteocyte-targeted drugs

Maria Veronica Lipreri¹, Gemma Di Pompo², Elisa Boanini³ , Gabriela Graziani², Enrico Sassoni⁴, Nicola Baldini^{1,2} and Sofia Avnet^{1,*} 

¹ Department of Biomedical and Neuromotor Sciences, University of Bologna, Bologna, Italy

² Biomedical Science, Technologies, and Nanobiotechnology Lab, IRCCS Istituto Ortopedico Rizzoli, Bologna, Italy

³ Department of Chemistry 'Giacomo Ciamician', University of Bologna, Bologna, Italy

⁴ Department of Civil, Chemical, Environmental and Materials Engineering, University of Bologna, Bologna, Italy

* Author to whom any correspondence should be addressed.

E-mail: sofia.avnet3@unibo.it

Keywords: osteocytes, microfluidics, hydroxyapatite nanoparticles, drug screening, 3D models, osteoporosis

Supplementary material for this article is available [online](#)

Abstract

Age-related musculoskeletal disorders, including osteoporosis, are frequent and associated with long lasting morbidity, in turn significantly impacting on healthcare system sustainability. There is therefore a compelling need to develop reliable preclinical models of disease and drug screening to validate novel drugs possibly on a personalized basis, without the need of *in vivo* assay. In the context of bone tissue, although the osteocyte (Oc) network is a well-recognized therapeutic target, current *in vitro* preclinical models are unable to mimic its physiologically relevant and highly complex structure. To this purpose, several features are needed, including an osteomimetic extracellular matrix, dynamic perfusion, and mechanical cues (e.g. shear stress) combined with a three-dimensional (3D) culture of Oc. Here we describe, for the first time, a high throughput microfluidic platform based on 96-miniaturized chips for large-scale preclinical evaluation to predict drug efficacy. We bioengineered a commercial microfluidic device that allows real-time visualization and equipped with multi-chips by the development and injection of a highly stiff bone-like 3D matrix, made of a blend of collagen-enriched natural hydrogels loaded with hydroxyapatite nanocrystals. The microchannel, filled with the osteomimetic matrix and Oc, is subjected to passive perfusion and shear stress. We used scanning electron microscopy for preliminary material characterization. Confocal microscopy and fluorescent microbeads were used after material injection into the microchannels to detect volume changes and the distribution of cell-sized objects within the hydrogel. The formation of a 3D dendritic network of Oc was monitored by measuring cell viability, evaluating phenotyping markers (connexin43, integrin alpha V/CD51, sclerostin), quantification of dendrites, and responsiveness to an anabolic drug. The platform is expected to accelerate the development of new drug aimed at modulating the survival and function of osteocytes.

Abbreviations

1, 25 D3 1, 25 dihydroxyvitamin D3
ATP Adenosine triphosphate
ALP Alkaline phosphatase
ab Antibody
2D Bi-dimensional
BSA Bovine serum albumin
Ca/P Calcium to phosphorous

Cx43 Connexion-43
Dkk1 Dickkopf WNT signalling pathway inhibitor 1
FBS Fetal bovine serum
HA-Nc Hydroxyapatite nanocrystals
HA Hydroxyapatite
Oc Osteocytes
OPG Osteoprotegerin
PTHrP Parathyroid hormone related protein

PTH	Parathyroid hormone
PBS	Phosphate buffered saline
RANKL	Receptor activator of nuclear factor kappa-B ligand
R°T	Room temperature
SEM	Scanning electron microscopy
Sost	Sclerostin
FCS	Fetal calf serum
3D	Three-dimensional
WNTs.	Wingless-related integration sites

1. Introduction

The Oc is the resident cell type within the bone tissue and constitute 95% of the total cell population of bone, with an average half-life of 25 years [1–3]. Oc reside in lacunae surrounded by the mineralised bone matrix, and are characterized by dendritic processes (40–60/cell), which protrude in small channels, forming a 3D lacuno-canalicular network. The Oc 3D dendritic network is known to act as a sensor for mechanical stimulation and to connect each single Oc with, surrounding elements, including other Oc, osteoblasts, blood vessels, nerve cells, and bone marrow cells [4–7]. Indeed, Oc are multifunctional and dynamic cells and through the development of the 3D dendritic network integrate hormonal signals and mechanical stimuli and, as a response, serve as a master regulator of bone remodelling and homeostasis. In these cells, fluid flow shear stress and molecular signals are sensed by specific receptors [e.g. PTH, PTHrP and 1,25-Dihydroxyvitamin D3, or pro-inflammatory cytokines [8]] that activate downstream signalling pathways or induce the release of paracrine factors to influence osteoblast and osteoclast functions, including cell differentiation, activity, and survival [1, 4, 6, 9]. The most studied signalling pathways and molecules are nitric oxide, prostaglandins, adenosine triphosphate, WNTs, (Dkk1, a pro-osteogenic Wnt pathway antagonist), receptor activator of nuclear factor kappa-B ligand (RANKL, the pro-osteoclastogenic factor), RANKL decoy receptor OPG, fibroblast growth factor-23, vascular endothelial growth factor, and sclerostin (Sost), that inhibits osteoblast function and differentiation [6, 10].

Nowadays, retaining Oc viability and activity is of paramount importance to maintain a healthy bone [2, 11], since its dysregulation can lead to reduced bone mass and bone fragility, and thus, to skeleton disorders, such as osteonecrosis, sclerosteosis, osteogenesis imperfecta, and osteoporosis [12, 13]. Oc functions can be altered by several common factors like the chronic use of drugs (e.g. glucocorticoids), some hereditary conditions, aging, inflammation [14], systemic diseases, such as diabetes [15], and even cancer [16]. Meticulous studies in the past 15 years have prompted the development of

innovative therapeutic agents that can treat these conditions, with an anabolic effect on bone, like antibodies against Sost (e.g. Romosozumab, Blosozumab) suggested for the treatment of osteoporosis [17], or teriparatide (PTH1-34) suggested for osteogenesis imperfecta and osteoporosis [18–22]. In particular, teriparatide has both an anabolic effect in osteoblasts and anti-apoptotic effects in Oc by targeting Wnt-1 inducible signalling pathway protein 2 and Sost signalling. However, currently available pro-anabolic drugs are very few and none are in experimental phase II or III. This may be partially due to the lack of adequate preclinical *in vitro* models that can recapitulate the 3D structure of the Oc network. Bidimensional models on 2D plastic, or 2.5D using collagen coating, are possibly too simplistic for the development of targeting approaches and may hide the risk of overestimated results about treatment efficacy as opposed to 3D models that bear the potential to be more predictive of drug response [23]. Per contra, cultivating Oc *in vitro* in 3D device is a real challenge.

To date, to recapitulate the 3D Oc microenvironment, several natural and synthetic matrices have been explored. In particular, to mimic the organic component of bone like polyethylene glycol hydrogels, collagen solution or collagen/Matrigel® blends, gelatin and gelatine methacrylate (GelMa) have been used [24–29]. To mimic the inorganic component of bone, which is primarily composed by nano-HA, ceramic scaffolds, like beads made of tricalcium or biphasic calcium phosphate, have been used. These have been directly seeded with cells or pre-coated with liquid collagen, and perfused with medium [30–33]. Despite the inherent advantages of these solutions, recapitulation of the 3D dendritic morphology has been difficult to achieve, suggesting the need of developing matrices to be combined with 3D devices that allow a homogeneous cell distribution over the matrix, adequate perfusion, and compatibility with cellular structures and functionality. On this regard, the combined use of 3D matrices and inorganic phase, or the culture of Oc in a perfused microfluidic channel filled with a crosslinked matrix has never been considered, or neither proposed for the set-up of large-scale microfluidic drug screening platforms [34]. In accordance with the European Union's regulation on the 3R rule (Replacement, Reduction, Refinement), the development of such a device would greatly reduce need for animal models that is currently the gold standard for the preclinical evaluation of new drugs [35, 36].

For the establishment of a screening platform for Oc-targeted drugs, the combination of collagenic extracellular matrix (ECM), with bone apatite, and shear-stress is also crucial since ECM stiffness/softening modulates the level of perfusion and, thus, determines the amount of drug that permeates

through the tissue and reaches the target [37, 38]. It also modulates the response to drugs through biological mechanisms by directly stimulating specific cellular signalling [39]. Furthermore, collagen, bone apatite and fluid flow shear stress promote viability and differentiation of osteogenic cells, including Oc [9, 40] and, thus, may indirectly change the activity of anabolic drugs. However, the development of a collagenic matrix that can be loaded in a microfluidic channel present some limitations and only a few matrices are available for this purpose [41]. Indeed, such a matrix should: (1) possess such physicochemical characteristics as to be biocompatible; (2) allow to be mixed with cells in liquid state; (3) allow the loading into microfluidic chambers; (4) allow its homogeneous distribution in the microchannel; (5) once loaded, become a gel without the use of cytotoxic crosslinking agents; (6) keep their characteristics till the end of the whole culture.

In this work, to mimic the network and the dynamic microenvironment of Oc for drug screening, we obtained an Oc dendritic network within a 3D microscaled bioreactor based on the use of a multi-chip microfluidic device. The cell-containing microchannels were filled with an osteomimetic matrix, enriched with Type I collagen and HA Ncs (HA-Nc), perfused and stimulated by shear stress, and then deeply characterised for the maintenance of Oc viability and expression of Oc specific markers as well as for drug response.

2. Experimental procedures

2.1. Preparation and loading in the microfluidic channel of matrix-embedded microspheres

2.1.1. Microfluidic support

To develop the dendritic network of Oc in a microfluidic platform, we used a multi-chip device with 96 chips (Two-lane OrganoPlate® device, 9605-400-B, Mimetas BV, Leiden, the Netherlands). Each chip consisted of two contiguous microfluidic channels with dedicated inlets and outlets, and an observation window that allowed real-time monitoring of the 3D culture (figure 1(a)). Channel A is dedicated to medium perfusion, while channel B is used to in-gel culture (figure 1(a)). The channels are separated by membrane-free PhaseGuide™ technology, allowing culture medium to diffuse from channel A towards the porous gel located in channel B. During the cell culture, the plate is placed on an interval rocker (Perfusion Rocker Mini, Mimetas), which tilts between a +7° and -7° inclination every 8 min. This creates bi-directional flow in the perfusion channel, resulting in pulsatile flow with a peak fluid shear stress (FSS) of 2.0 dyne cm⁻² [42], and ensures constant oxygen and nutrient exchange. As a result, continuously exposed to culture medium diffusion from the perfusion channel, while cells at the interface between

the two channels are subjected to FFS. We also conducted a permeability assay with FITC-dextran (20 KD) fluorescent solution to qualitatively confirm culture medium diffusion from the perfusion channel to the in-gel culture channel (supplementary figure 1). The model was designed so that the cells-enriched matrix blend could be loaded in a liquid state, into the microchannel and patterned using a surface tension technique called phase guiding [43]. Following this technique, after matrix thermal-crosslinking at 37 °C, the culture medium could be injected in the adjacent microchannel A, allowing for membrane-free perfusion which is crucial to maintain cell viability and the formation of the Oc dendritic network [44].

2.1.2. Collagenic matrix

To reproduce the organic component of bone ECM, we chose Matrigel® (Corning, New York, USA) and Cultrex™ 3D Culture Matrix Rat Collagen (from now on Cultrex™, R&D systems, Minneapolis, MN, USA). Unlike other hydrogels, they can be processed under mild conditions that are compatible with cell viability, because: (i) once loaded in the microfluidic channel, their gelation occurs in a short time (15 min), thus avoiding cells deposition on the bottom of the channel; (ii) the gelation of the hydrogels is temperature-dependent and does not require toxic reagents. For Matrigel®-mixtures, we diluted the pure Matrigel® at 90% or 75%. For material characterization, Matrigel® was diluted with PBS, while for the subsequent biological characterization Matrigel® was diluted with rat tail collagen type I, 0.01% v/v in PBS. For Cultrex™, 1 M HEPES, pH 8.0, 37 g l⁻¹ NaHCO₃ and an 8.44 mg ml⁻¹ rat tail collagen type I were mixed at 1:1:8 ratio to a final collagen concentration of 4.0 mg ml⁻¹. The gel were then loaded through the gel inlet of channel B in the Two-lane OrganoPlate® device (9605-400-B, Mimetas BV, Leiden, the Netherlands). The plate was incubated at 37 °C for 15 min to allow gelation of the matrix. After gelation, a total of 150 µl of cold alpha Minimum Essential Medium (αMEM, Sigma) supplemented with 2.5% FCS and 2.5% FBS added with 1% penicillin/streptomycin was added to the medium inlet and outlet. Perfusion was started by placing the device on an interval rocker (Perfusion Rocker Mini, Mimetas) switching between a +7° and -7° inclination every 8 min (37 °C, 5% CO₂) thus allowing bi-directional flow to achieve perfusion of the medium through the chip. Medium was refreshed every three days post-injection

2.1.3. HA Ncs

We added different amounts of stoichiometric HA-Nc. HA-Nc were synthesized and characterized as previously described [45, 46]. HA-Nc have mean dimensions of about 200 nm × 40 nm and are biocompatible when cultured with endothelial cells

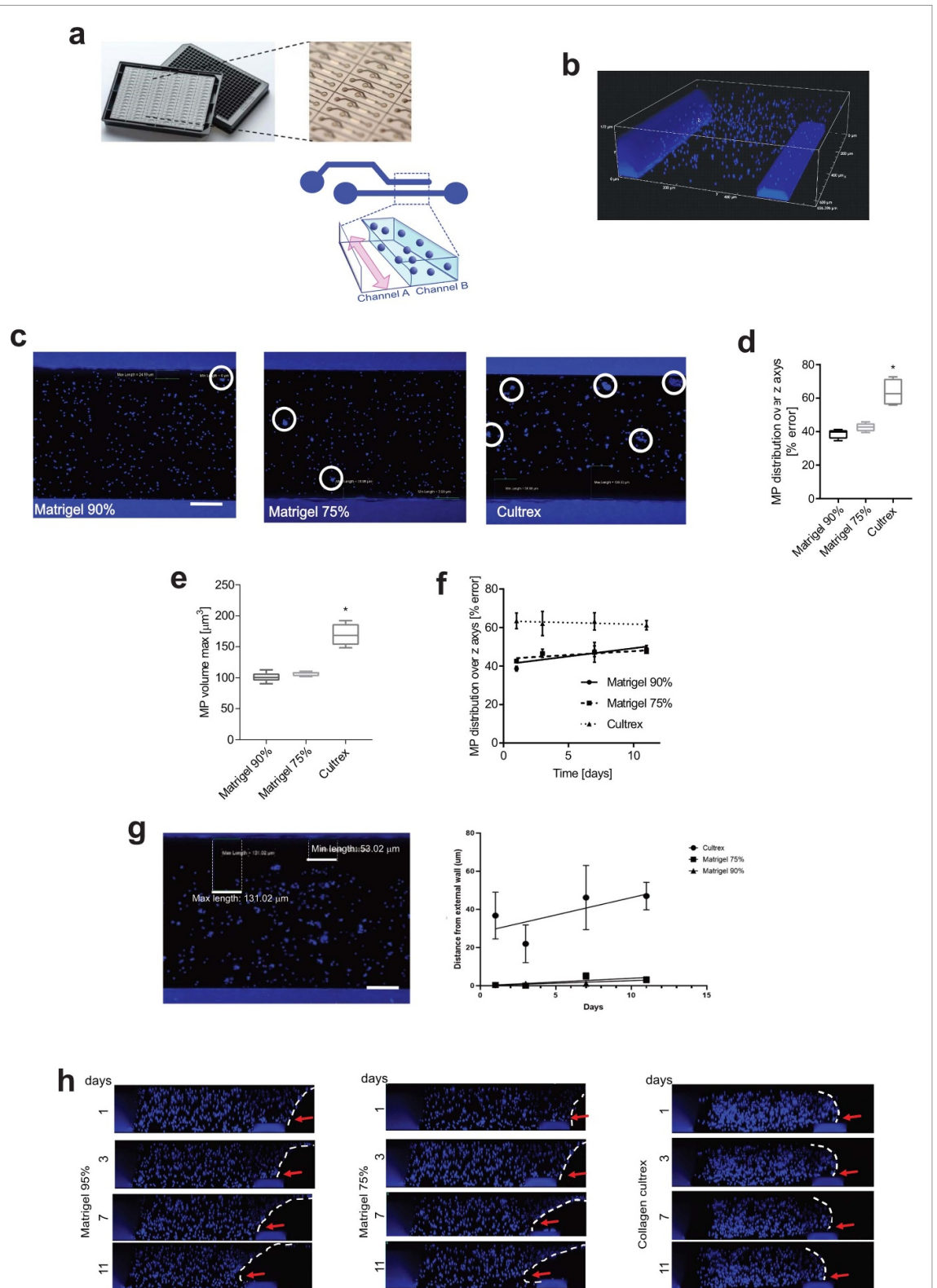


Figure 1. Set-up of the microfluidic model and of the matrix blend of 3D Oc cultures. (a) 2-chip microfluidic plate used in this study and schematic representation of the perfused channel A and the channel B used for the hydrogel injection mixed with fluorescent microspheres (MP) or cells. (b) Volume render of the confocal acquisition of channel B injected with hydrogel mixed with MP. (c) Merge of 86 z-scans of representative chips for each of the tested different types of hydrogel, used for the quantification of clusters (white circles). (d) Graph of the fluorescent microspheres distribution over the z axis 24 h after the hydrogel injection (as evaluated by the percentage error of n of microspheres/scan). (e) Box-plot graph of the volume of clusters of microspheres or single microspheres as an index of the tendency of microspheres to form clusters within the specific hydrogel. (f) Graph of the microsphere distribution over the z axis over time (as evaluated by the percentage error of n of microspheres/scan). (g) In the upper panel, merge of 86 μx -scans of a representative chip to show the distance of the matrix from the external wall of the channel B, as a measure of the retraction of the matrix over time; in the lower panel graph of the measured distance from the external wall of the channel B, of the microsphere-containing matrix over time. (h) Merge of z-scan of channel B to show matrix retraction and surface degradation at the gel/liquid meniscus (white dotted line) over time (red arrow, point of erosion).

[45]. We diluted autoclave sterilized HA-Nc powder in the Type I collagen solution that was then used to prepare the matrix mixture as described in § 2.1.1. We then ultrasonicated the HA-Nc solution for 10 min at R°T. We used a HA-Nc concentration to reach a final value of 0.1-0.2-0.4-0.8% (w/v) in the injected matrix mixture, that was prepared as described in § 2.1.1.

2.2. Characterization of the technical parameters of matrix mixtures

2.2.1. Dispersion of autofluorescent microspheres within the matrix

For each chip, we pelleted 20.000 Tetraspeck™ TM Microspheres (Life Technologies, Carlsbad, CA, USA) by centrifugation at 8 xg for 5 min, and then we resuspended with 2.3 µl of each matrix mixtures (Matrigel® 75%, Matrigel® 90%, Cultrex™), separately. The microspheres-enriched matrices were loaded in the gel channel (channel B) in the microfluidic device, as previously described (§ 2.1.2). As a measure of microsphere dispersion, we detected the fluorescent signal of Tetraspeck™ TM Microspheres within the microchannel B (figure 1(b)). For image acquisition of channel B, after 1-3-7-11 d of incubation, we used A1R MP confocal microscope (objective 20× air, numerical aperture 0.75, refractive index 1, Resonant scanning, zoom at 1, z-step 2 µm, 86 Z-stack loops with Ni-E ZDrive, Nikon). For the excitation, we used 402.7 laser power at 6.7, PMT HV 117, PMT Offset 0, pinhole size 14.05 µm, and scan speed 7.5. For the analysis and automatic quantification, we used NIS Elements AR 5.40.01. As an index of microsphere dispersion, we used the percentage error (standard deviation × 100/absolute value) of n of microspheres/scan (n = 86 scan), in five different chips for each condition. For this assay, we used the 'Define threshold' and 'Perform measurement' functions.

2.2.2. Cluster formation of autofluorescent microspheres within the matrix

The same images, acquired as described in § 2.2.1, were used to quantify the tendency to form clusters of microspheres. As an index, we used the max volume of the detected objects. For the automatic measurements, we used the '3D threshold' and '3D object measurement' functions. For each condition, we measured 5 different replicates.

2.2.3. Matrix retraction and surface degradation

The same images, acquired as described in § 2.2.1 at 0-1-3-7-11 d, were used for the quantification of the tendency of matrix to retract and degrade at the surface. As an index, we used the distance of the first fluorescent signal, coming from the microspheres, detected from the edge of the outer side wall of the B-channel towards the phase guide, as manually measured. For each condition, we measured five different replicates.

2.2.4. Electron microscopy analysis

HA-Nc dispersion within Matrigel® 75% was evaluated by SEM analysis. This analysis has been performed on macroscale bulk samples of Matrigel® 75% diluted with Type I collagen (Sigma), with (0.1-0.2-0.4-0.8% w/v), and without HA-Nc. Matrices were prepared as described in § 2.1.1 and § 2.1.2, and, for each sample (n = 2 samples per condition), 500 µl of blend were dispensed dropwise in a 24-wellplate. The plate was then incubated at 37 °C for 15 min to allow gelation of the matrix. Samples were fixed with 2% glutaraldehyde (Merk, Darmstadt, Germany) in 0.1 M sodium cacodylate buffer (Sigma), and washed in 0.1 M sodium cacodylate buffer. Complete dehydration was achieved in graded alcohol series and hexamethyldisilane tetroxide (Electron Microscopy Sciences, Hatfield, PA, USA). Samples were sputter-coated with gold and observed by a field emission gun scanning electron microscope (FEG-SEM, Tescan Mira3, CZ, working distance = 10 mm, voltage = 5 kV).

2.2.5. Rheological characterization

We performed amplitude sweep test, frequency test, and viscosity evaluation on all samples (Cultrex™, Matrigel 90%, Matrigel 75% and Matrigel 75% with nanoparticles of HA 0.1% w/v) at both 4 °C and 37 °C. The temperature of 4 °C represents the gel's temperature during loading into the microfluidic channel before the thermal gelation process begins, while 37 °C represents the temperature during cell culture. The amplitude sweep was conducted at a fixed frequency of 1 Hz for Cultrex™ and 0.3 Hz for Matrigel samples for the measurement performed at 4 °C, while a frequency of 1 Hz was applied at all the measurements performed at 37 °C. In both conditions, the shear stress range applied for the linear viscoelastic region (LVER) determination was 0.01–100 Pa. The frequency Sweep Test was performed in the LVER, where the structural integrity of the material is not affected. The test was conducted in the range of 0.01–10 Hz and at a fixed shear stress of 0.1 Pa for Cultrex™ and Matrigel 90% samples and 0.05 Pa for the Matrigel 75% samples in the measurements at 4 °C. In the measurements at 37 °C the shear stress was of 1 Pa for all samples. The viscosity of the material was determined as a function of the applied shear stress. The measurements were performed in the range of absolute value of shear of 0.1–1000 1/s for both Cultrex™ and Matrigel samples at 4 °C and 37 °C. The rheological test were performed as an external service by an external service (Alphatest Lab, Italy).

2.3. Cell cultures

2.3.1. 2D cultures

Murine MLO-Y4 and MLO-A5 Oc-like cells deriving from Oc primary cultures were obtained from Kerfast (Boston, MA, USA). These cells have been

extensively characterized and express specific Oc morphology, behaviour and markers [47, 48]. MLO-Y4 cells were maintained in alpha-MEM medium supplemented with 2.5% FCS, 2.5% FBS, and 1% penicillin/streptomycin, whereas MLO-A5 cells were maintained in alpha-MEM medium supplemented with 5% FCS, 5% FBS, and 1% penicillin/streptomycin. Cells were cultured only up to the 40 passages. For 2D experiments, cells were seeded on eight-well chamber slides pre-coated with 0.01% v/v rat tail Type I collagen in PBS (Sigma). Medium was changed every three days.

2.3.2. 3D cultures

For 3D microfluidic and perfused cultures, MLO-Y4 and MLO-A5 cells were detached for 2D support when at semi-confluence (70%), washed with PBS and counted. Pelleted cells were resuspended in Matrigel[®] 75% and loaded in the gel channel of the Two-lane OgranoPlate[®] device (9605-400-B, Mimetas BV) (10.000 cells/chip). To choose the optimal dilution solution to obtain Matrigel[®] 75%, we assayed the effect on cell viability of Matrigel[®] diluted with: (i) culture medium, (ii) rat tail collagen type I from Sigma (#C-7661), 0.01% v/v in PBS, (iii) neutralised Cultrex[™] 0.01% v/v in PBS.

2.4. Cell viability and cytotoxicity

2.4.1. Live-dead assay with automated scanner (confocal microscope)

The cell viability was determined using the LIVE/DEAD[™] Cell Imaging Kit (# R37601, Thermo Fisher Scientific, Waltham, MA, USA), according to the manufacturer's protocols. Briefly, for 2D samples, cells were washed once with PBS and then incubated with the live/dead staining mixture for 15 min at 37 °C in the dark. After incubation, cells were washed once again with PBS and then observed by confocal microscopy. For image acquisition of channel B, we used AIR MP confocal microscope (objective 20× air, numerical aperture 0.75, refractive index 1, Resonant scanning, zoom at 1). For the excitation, we used 487.2 laser power at 5.0, PMT HV 14, PMT Offset 0, and 561.3 laser power at 1.2, PMT HV 43, PMT Offset 0, pinhole size 58.75 μm, line average 4, scan speed 7.5. For the analysis and automatic quantification, we used NIS Elements AR 5.40.01 and the 'bio analysis' application and 'cell count analysis' function.

For 3D samples, matrix-embedded cells within the microchannel B were washed once with PBS (200 μl total volume added in the inlets and outlets) and then incubated with the live/dead staining mixture (110 μl total volume added in the inlets and outlets) for 20 min at 37 °C in the dark. After incubation, cells were washed once again with PBS as described above, and then observed by manual confocal microscopy. For image acquisition of channel B, we used AIR MP confocal microscope (objective

20× air, numerical aperture 0.75, refractive index 1, Resonant scanning, zoom at 1, z-step 6 μm, 30 Z-stack loops with Ni-E ZDrive, Nikon). For the excitation, we used 487.2 laser power at 6.0, PMT HV 44, PMT Offset 0, and 561.3 laser power at 2.5, PMT HV 43, PMT Offset 0, pinhole size 57.47 μm, line average 4, and scan speed 7.5. For the analysis and automatic quantification, we used NIS Elements AR 5.40.01. For automatic cell count, we used the '3D threshold' and '3D object measurement' functions. We then calculated the percentage of viable cells (green) with the following equation: $[(n. \text{ of green objects}) \times 100] / (n. \text{ of green objects} + n. \text{ of red objects})$. For both types of cultures, we calculated the percentage of viable cells (green) with the following equation: $[(n. \text{ of green objects}) \times 100] / (n. \text{ of green objects} + n. \text{ of red objects})$, and measured 8 different replicates for each condition.

2.4.2. Calcein-AM/Hoechst33342 assay with automated cell imaging system (fluorescent inverted microscope)

MLO-Y4 cells were detached for 2D support when at semi-confluence (70%), washed with PBS, counted, and mixed with Matrigel[®] 75% (diluted with Type I collagen, Sigma, and with HA-Nc at 0.1% w/v), and then loaded in Two-lane OrganoPlate[®] device (10.000 cells/chip). After 24 h, we added to the medium dexamethasone [1×10^{-6} or 3×10^{-6} M] (Sigma), with or without teriparatide [100 nM] (Sigma). After additional seven days, we incubated cells with calcein-AM (Molecular Probes) and Hoechst33342 (Sigma) for the staining of live and dead cells. For automated image acquisition and analysis we used ImageXpress (objective 4×, Molecular Devices, San Jose, CA, USA). Cells that were positive for both calcein-AM and Hoechst33342 (co-localization of green and blue, respectively) were considered as live cells. Cells that were stained only for Hoechst33342 were considered as dead cells (blue only). For the automatic cell counting we used the CellReportXpress software (Molecular Device). We performed 14 replicates for each conditions.

2.4.3. Annexin-V assay with automated cell imaging system (fluorescent inverted microscope)

MLO-Y4 cells were detached from the 2D support when at semi-confluence (70%), washed with PBS, counted, and mixed with Matrigel[®] 75% (diluted with Type I collagen, Sigma, and with HA-Nc at 0.1% w/v), and then loaded in Two-lane OgranoPlate[®] device (10.000 cells/chip). After 24 h, we added to the medium dexamethasone [3×10^{-6} M] (Sigma), with or without teriparatide [100 nM] (Sigma). After additional six days, we performed the Annexin-V assay on live cells, according to the manufacturer protocol with few modifications (#V13245, Molecular Probes, Eugene, OR, USA). Briefly, matrix-embedded cells within the microchannel B were washed once with

PBS (200 μl total volume added in the inlets and outlets) and then incubated with the Alexa Fluor 488 Annexin V/PI/binding buffer solution (70 μl total volume added in the inlets and outlets) for 15 min at 37 °C in the dark. After washing with PBS, for automated image acquisition and analysis we used ImageXpress Pico and CellReportXpress software (objective 4 \times , Molecular Devices). We performed 8 different replicates for each condition.

2.5. Immunofluorescence

After three days of culture as described in § 2.3, both 2D and 3D samples were washed once with PBS, then fixed in 100% cold methanol, and blocked with 1% BSA. As primary antibodies, we used anti-connexin-43 (Cx43) rabbit polyclonal Ab (#ab11370, Abcam, Cambridge, UK) and anti-CD51 rabbit polyclonal Ab (#ma5-32195, Invitrogen, Waltham, MA, USA). As secondary antibodies, we used anti-mouse or anti-rabbit Alexa Fluor 488 nm antibodies (Life Technologies). For the staining of polymeric actin (*F*-actin), we used phalloidin-TRITC (Sigma, 0.5 $\mu\text{g ml}^{-1}$). Nuclei were stained with Hoechst 33258 (Sigma).

2.6. Dendrite elongation assay with automated scanner (confocal microscope)

To evaluate the formation of a dendritic network in 3D cultured Oc, we cultured, fixed, and stained the cells as described in § 2.5. For the visualization and quantification of the formed dendrites in the 3D Oc network, we stained with the anti- β -actin rabbit polyclonal Ab (#4970 Cell Signalling, Danvers, MA, USA) that stains the total β -actin protein (both G and F- forms) that is spread through the cytosol. As secondary antibodies, we used the anti-rabbit antibody Alexa Fluor 488 nm (Life Technologies). Nuclei were stained with Hoechst 33258. For image acquisition of channel B, we used A1R MP confocal microscope (objective 20 \times air, numerical aperture 0.75, refractive index 1, Resonant scanning, zoom at 2, z-step 1.75 μm , 93 Z-stack loops with Ni-E ZDrive, Nikon). For the excitation, we used 402.7 laser power at 7.7, PMT HV 89, PMT Offset -24, and 487.2 laser power at 10.6, PMT HV 70, PMT Offset 0, pinhole size 63.86 μm , line average 4, and scan speed 7.5. For the analysis and automatic quantification, we used NIS Elements AR 5.40.01 and, as a parameter to evaluate the average length of the branches of the cellular network, we used the 'average length major axis of branches'. This was automatically calculated by using in the 'Binary setting', among the 3D Processing/Morphology commands, the 'skeletonize' function (supplementary video 1). After this image pre-processing, we applied the automatic measurement of 3D objects. For each chip, we quantified three different fields, and we replicated each condition for 6 different chips.

2.7. RNA isolation and Q-RT-PCR

MLO-Y4 cells were cultured in 2D and 3D conditions, as described in § 2.3. For 2D condition, cells were cultured in 24-well plates precoated with rat tail Type I collagen 0.01% v/v in PBS. For 3D conditions, cells were cultured in a Two-lane OrganoPlate® device (9605-400-B, Mimetas BV) (10,000 cells/chip) within the osteomimetic matrix (with HA-Nc at 0.1% w/v) or in the collagenic matrix w/o HA-Nc. After two days of culture, total RNA was extracted from both the 2D and 3D cell cultures using TRIzol reagent (Invitrogen, Thermo Fisher Scientific). For 2D cultures, TRIzol was added directly to cells to obtain cell lysates. For 3D cultures, to obtain single-cell suspensions from matrices, the cell/matrix mix that was extracted from the microfluidic channel was preliminarily digested using the Tumor Dissociation Kit, in combination with the gentleMACS Octo Dissociator (Miltenyi Biotec). The dissociated cells were then passed through a 30 μm diameter filter (Miltenyi Biotec) to remove any residual matrix, centrifuged, and lysed in TRIzol. For both 2D and 3D cultures, total RNA was reverse transcribed with MuLV reverse transcriptase (Applied Biosystems, Thermo Fisher Scientific). Real-time Polymerization Chain Reaction (Real-time PCR) was then performed to analyse specific gene expression by amplifying 500 ng of cDNA using the CFX96Touch instrument (Biorad) and the Universal Probe Library system (Roche Applied Science). Probes and primers were selected using the web-based assay design software (ProbeFinder: www.roche-applied-science.com) (table 1). Results were normalized to TATA-box binding protein according to the $2^{-\Delta\Delta\text{CT}}$ method.

2.8. ALP assay

Oc were cultured in 2D and 3D conditions, as described in § 2.3. After seven days of culture, cytochemical staining for alkaline phosphatase activity (ALP) was performed using a commercial kit (Leukocyte Alkaline Phosphatase Kit, Sigma).

2.9. HA-Nc cellular uptake

2.9.1. Confocal microscope

MLO-Y4 cells were cultured in 2D conditions as described in § 2.3.1. We added HA-Nc 0.1% w/v to the cell supernatant and incubated it for three days in standard culture conditions. The internalization of HA-Nc was analysed by confocal microscopy (A1R MP confocal microscope) and by taking advantage of HA-Nc autofluorescence. In particular, we use laser 561.3 (power 19.2, gain 9, pinhole 43.42, emission 611.2-661.2 λ , Galvano scanner, objective 60 \times oil, numerical aperture 1.4, refraction index 1.515, z-step 0.3 μm , 44 Z-stack loops with Ni-E ZDrive, scan speed 0.25, line average 2).

Table 1. Probes and primers.

Gene	Full name	Accession Number	Primers	Probe
TBP (<i>Mus Musculus</i>)	TATA-box binding protein	NM_013684.3	<i>F</i> = ggcggtttggctaggttt <i>R</i> = gggttatcttcacacacatga	107
Cx43 (<i>Mus Musculus</i>)	Connexin 43 (alpha-1 gap junction)	M63801.1	<i>F</i> = agcccgaactctcctttct <i>R</i> = cgctccagtcacccatgt	75
SOST (<i>Mus Musculus</i>)	Sclerostin	AF326740.1	<i>F</i> = tcctgagaacaaccagacca <i>R</i> = ggcgtcataggatgggtg	16

2.9.2. SEM

MLO-Y4 cells were cultured in 2D conditions on rounded cover slides (diameter 6 mm) that were pre-coated with Type I collagen. Cover slides with cells were then inserted in a 48-well plate and cultured as described in § 2.3.1. Cells were then cultured as described in § 2.3.1. After 24 h from seeding, we added HA-Nc 0.1% w/v to the cell supernatant and incubated for three days in standard culture conditions. Cells were then washed and fixed with 2% glutaraldehyde (Merk) in 0.1 M sodium cacodylate buffer (Sigma), washed in 0.1 M sodium cacodylate buffer, and post-fixed in 1% osmium tetroxide (Electron Microscopy Sciences) in 0.1 M sodium cacodylate buffer. Complete dehydration was achieved in graded alcohol series and hexamethyl-disilane tetroxide (Electron Microscopy Sciences). Samples were sputter-coated with gold and observed by a FEG-SEM (Tescan Mira3, CZ, working distance = 10 mm, voltage = 10 kV).

2.10. Statistical analysis

Because of the small number of observations, we did not consider the data normally distributed and therefore used non-parametric tests. For statistical analyses, we used GraphPad Prism 7.0 software (GraphPad Software). For differences between the two groups, we used the two-tailed Mann-Whitney U test; for the analysis of correlation, we used the Spearman test (one-tailed). For all the experiments, we expressed values as the mean \pm standard error of the mean (SEM) and considered only $p < 0.05$ values statistically significant.

3. Results

3.1. Matrigel®/type I collagen blend is the optimal injectable matrix to culture Oc in the perfused microchannel

To mimic *in vitro* the ECM of Oc, we chose among two different injectable organic matrices and dilutions: Matrigel® 90%, Matrigel® 75%, and Cultrex™. We selected the best type of matrix and dilution based on the capacity to allow an optimal cell distribution within the matrix after the loading in the microfluidic channel and based on the stability of

the matrix structure after prolonged passive perfusion. However, to characterize an injectable matrix that gelate in situ, in a ‘closed’ microchip, is a difficult task. Therefore, to observe and analyse the 3D distribution of Oc cell-bodies-sized objects (Oc cell-body diameter 5–20 μm [49]) within the matrix, over time, and to visualize the borders of the matrix (used here to indirectly assess surface degradation), we used commercial autofluorescent microspheres (diameter 4 μm), that can be easily detected by confocal microscope (figure 1). First, 24 h after matrix injection, we observed a homogeneous z -axis distribution of the microspheres in both Matrigel® 90 and 75%. In contrast, for Cultrex™, we observed a greater tendency to form clusters of microspheres, measured as the tendency to form larger fluorescent objects, and a greater percentage error in the number of microspheres/s-can (figures 1(c)–(e)). In addition, as a measure of durability and stability in a shear-stressed and perfused environment, we also quantified the maintenance of the distribution of the microspheres in the z -axis over time (figure 1(f)), the distance of the first fluorescent signal detected from the edge of the outer side wall of the B-channel towards the phase guide (figure 1(g)), and also the changes in the shape of gel/liquid (matrix/medium) meniscus, at the boundary between channel A and B, over time, which could be discerned from the fluorescence signals of the microspheres dispersed in the matrix (figure 1(h)). These analyses showed that Cultrex™ tended to shrink and form a solid, compact clot, which was not eroded by the constant perfusion of the medium and yet detached from the wall of channel B, and invaded the adjacent channel A, as the days passed. Indeed, the z -axis dispersion of microspheres in the Cultrex™ matrix remained unchanged over time, suggesting that the microspheres did not move from their original position. The Matrigel®-based mixtures, on the other hand, did not detach from the side wall and showed a slow and gradual erosion of the meniscus profile, but without drastically damaging the structure and pattern of the matrix, at least up to ten days of culture. We do not know whether these different matrix behaviours were due to volume collapse, stiffness differences, or phase transition, but based on these characteristics, Cultrex™ was not used further and we selected the 75% Matrigel® for subsequent

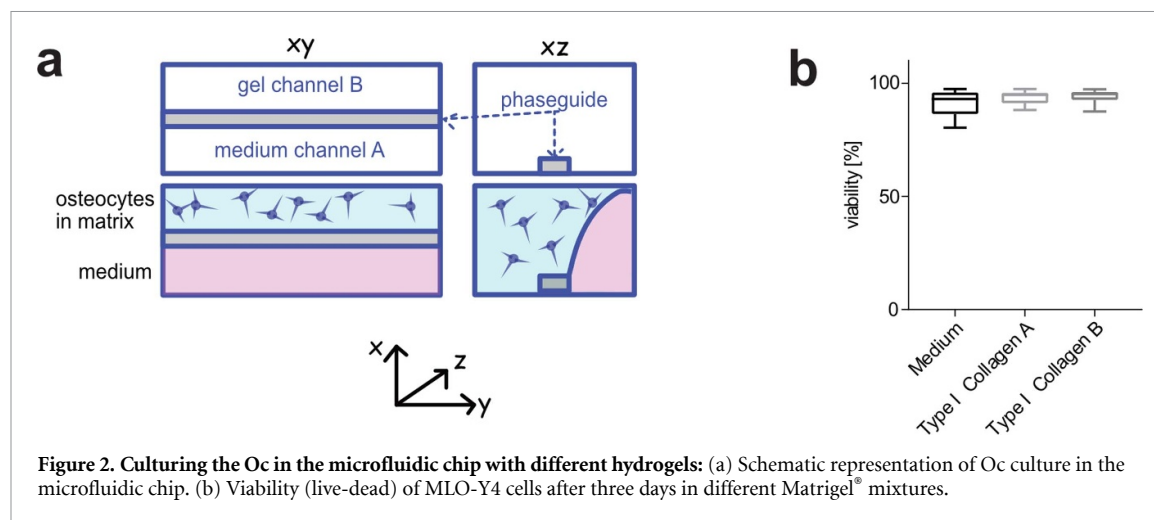


Figure 2. Culturing the Oc in the microfluidic chip with different hydrogels: (a) Schematic representation of Oc culture in the microfluidic chip. (b) Viability (live-dead) of MLO-Y4 cells after three days in different Matrigel[®] mixtures.

experiments. Indeed, the parameters of Matrigel 75% were almost the same as those of 95% Matrigel[®], but it had better manual injectability and showed fewer microspheres dispersion over time (at 11 d vs 1 d, for Matrigel[®] 75% $*p = 0.0159$, for Matrigel[®] 90% $**p = 0.0079$). To improve Oc viability and dendritic network formation, we also considered different liquid collagen solutions for matrix mixing and compared their effect on Oc viability in the microfluidic device (figure 2(a)): in terms of viability, all the conditions analysed did not differ significantly in respect to the normal culture medium (figure 2(b)). The final blend we used from here on was Matrigel[®] diluted 75% in a 0.01% v/v Type I collagen solution in PBS.

3.1.1. Rheological characterization of the gels

The rheological tests performed on Cultrex[™], Matrigel 90% and Matrigel 75% gave information on LVER of the gels, their viscoelastic response, the elastic modulus and the viscosity. The larger LVER, that means more stability to the deformation stress, was achieved in the test performed at 37 °C, probably due to the cross-linking of the samples that occurs during the loading on the warm plate (supplementary figures 2(a) and (b)). Moreover, at 37 °C the phase angle δ indicates a ‘solid like’ behaviour for all the samples tested (values $<45^\circ$, supplementary figure 2(b)). On the other hand, in the tests at 4 °C, all the Matrigel-based samples show a $\delta > 45^\circ$, indicating a ‘liquid like’ behaviour, except for the Cultrex[™] sample ($\delta < 45^\circ$, supplementary figure 2(a)). According to these results, at 4 °C Cultrex[™] exhibit a wider LVER and a complex shear stress modulus G^* two orders of magnitude higher than Matrigel based gels. The frequency sweep test confirms the previous observations comparing the measurement at 4 °C and 37 °C: in the latter condition, all samples show an elastic behaviour quite stable in the measurement range, with a

phase angle $\delta < 45^\circ$. In the tests at 4 °C, only Cultrex[™] sample shows a $\delta < 45^\circ$. On the contrary, the Matrigel samples exhibit the predominance of viscous behaviour, with a phase angle $\delta > 45^\circ$. These last samples seem to not well support the shear stress applied and/or the geometry in the range of frequency above 1 Hz. The crossover frequency marks the transition from viscous to elastic behaviour, as shown by the G' and G'' modules in supplementary figure 2(c) and by the drift of the phase angle. The same sample analysed at 37 °C (therefore crosslinked) shown a predominant elastic behaviour throughout the measuring range, as reported in supplementary figure 2(d). The viscosity curves performed at 4 °C define the macroscopic differences observed between the samples. Cultrex[™] was the higher viscosity sample, while the viscosity decreases with the dilution applied in the Matrigel-based samples (supplementary figures 3(a) and (b)). In the case of test performed at 37 °C the range of values recorded appears narrow down, probably by the cross-linking of samples that occurs during the loading (supplementary figure 3(b)).

3.2. MLO-Y4 morphology is different in 3D vs 2D cultures, whereas viability is unaffected

To assess the viability of the 3D Oc culture, we used both fully differentiated Oc cells (MLO-Y4) and pre-Oc (MLO-A5) cells. At both three and seven days, the percentage of live MLO-Y4 cells remained very high (over 90%), and comparable to that obtained under 2D conditions. For the MLO-A5 cells, this was only the case at three days, since at seven days, in the 3D microchannel, cells had probably grown too much and the conditions had become too stressful (figures 3(a) and (b)).

To evaluate the different morphology and the formation of focal adhesions, we fixed and immunostained MLO-Y4 cells under different conditions (figure 3(c) and supplementary figure 4). We compared: (1) adherent cells on a static 2D support,

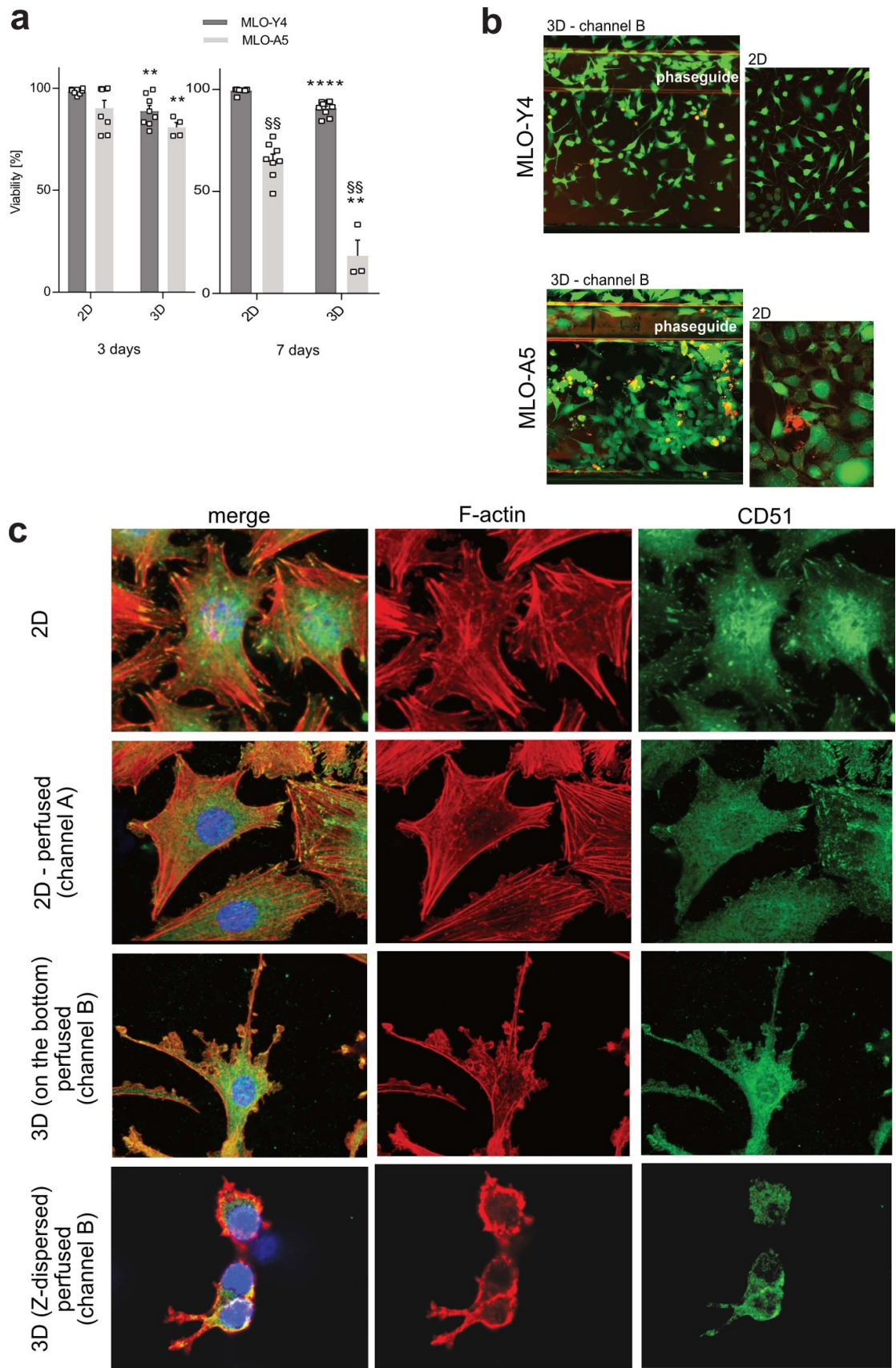


Figure 3. Osteocytes embedded in Matrigel®/Type I collagen blend and perfused in the microchannel are fully viable and showed a 3D dendritic morphology. (a) Cell viability (live-dead) of MLO-Y4 and MLO-A5 cells in 2D vs 3D conditions (** $p < 0.01$, **** $p < 0.0001$ vs 2D; $^{ss}p < 0.01$ vs MLO-Y4). (b) Representative image of live-dead assay in (a), at three days. (c) Immunofluorescence staining of *F*-actin (TRITC/red) and CD51 (FITC/green), an osteocyte marker that localised at dendritic level, to highlight the formation of adhesion structures and dendrites at three days of cultures in 2D not perfused (standard plate), 2D perfused (channel A in the microfluidic plate), 3D on the base of matrix-embedded (channel B in the microfluidic plate) and in the middle (*z*-dispersed) of the same channel. Nuclei were counterstained with Hoechst33 258. Images were acquired by confocal microscope (objective 20 \times).

according to standard culture conditions (2D); (2) adherent cells that migrated from the channel B to the base of channel A of the microfluidic chip during the culture (2D-perfused); (3) adherent cells of the base of channel B, embedded in the matrix (3D-on the base-perfused); (4) non-adherent cells dispersed on the z-axis within the matrix, in channel B. The cytoskeleton was completely different between the non-adherent and adherent cells: 3D dendritic network structures were visible only in the non-adherent condition, whereas in the 3D (on the base) perfused condition, only 2D dendrites could be observed. On the other hand, focal adhesion sites, with co-localization of integrin- μ V (CD51) and *F*-actin, at the end of stress-fibres, appeared only in 2D, both in perfused and non-perfused conditions. Notably, focal adhesions appeared more numerous under shear-stressed conditions. At the base of channel B, this type of focal adhesions was replaced by small membrane protrusions along the tubule-like dendrites, in combination with a clear rearrangement of the cytoskeleton and a change in morphology. Finally, in the 3D-dispersed cells, co-localization of *F*-actin and integrin- μ V appeared both in dendrite-like protrusions and near to the cytoplasmic membrane in the Oc cell body.

3.3. The expression of Oc markers is increased in the 3D perfused and matrix-embedded microchannel

We then compared the expression of markers that increase in fully differentiated Oc, such as Cx43, a major gap-junction protein that plays a crucial role in the formation of Oc networks [44], and Sost, a glycoprotein produced by Oc that antagonizes the Wnt pathway [10]. By immunofluorescence staining, we observed a spot-like localization of Cx43 in the junctions of the 3D network, between one Oc and another, interconnected and embedded in the matrix within the microfluidic chip (figures 4(a) and (b)). Furthermore, the signal intensity of Cx43 appeared higher in 3D cultures than in 2D cultures, especially for MLO-Y4 cells. The Cx43 protein also appeared redistributed from the perinuclear region to the cytoplasm and dendritic processes, again, especially in MLO-Y4 cells. We observed a trend towards increased expression of Cx43 in 3D Oc also by the analysis of mRNA, isolated from cells recovered from the microfluidic channel, compared to cells cultured under standard conditions (figure 4(c)). Remarkably, Sost, which is usually not expressed in 2D cultured of MLO-Y4 cells [50], as also observed in our cultures, was significantly induced in 3D (figure 4(c), $**p = 0.0043$). Perfusion and inclusion in the matrix also strongly promoted the expression of alkaline phosphatase, an additional marker of the Oc phenotype, as was clearly revealed by the comparison with

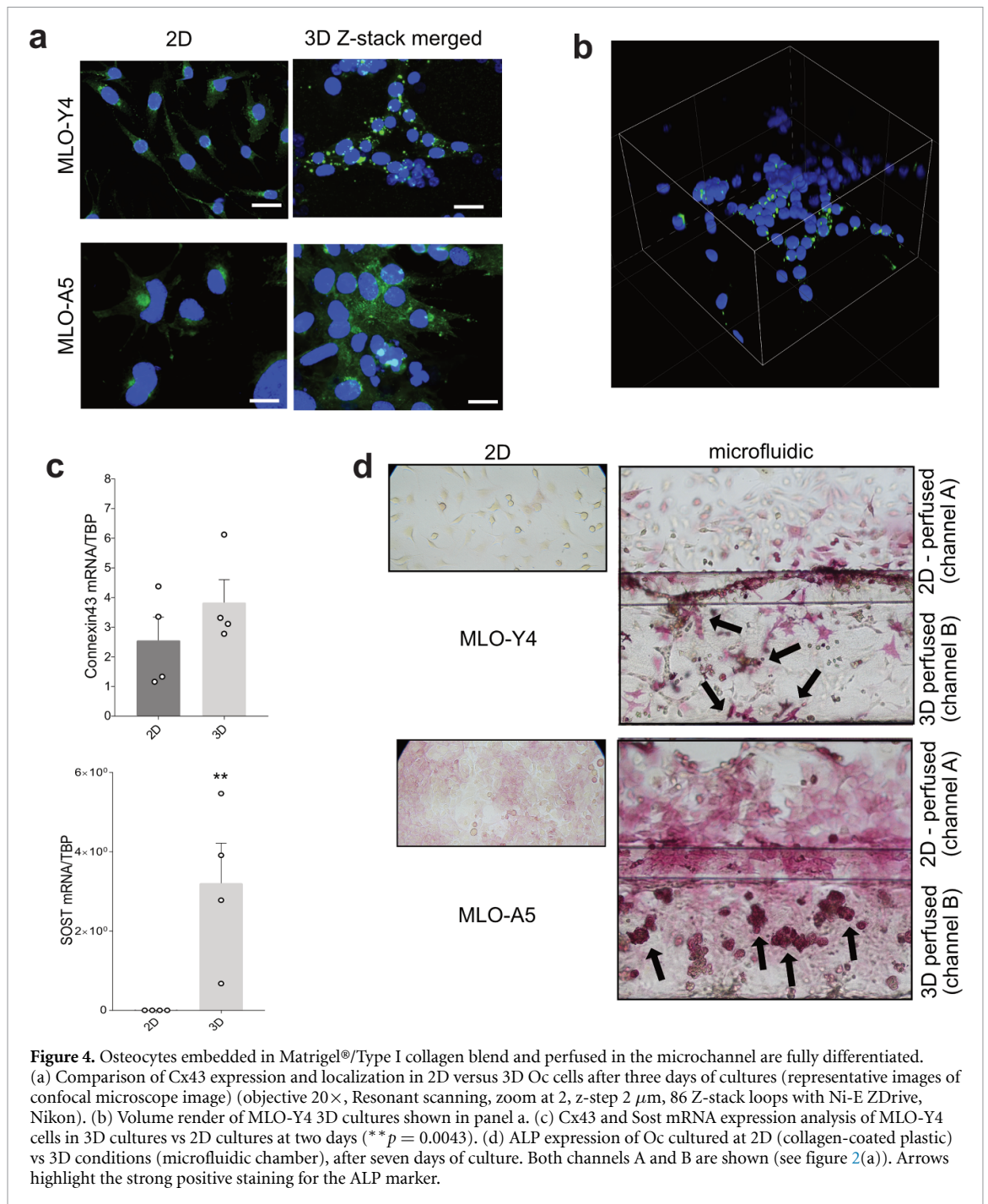
the 2D perfused condition (channel A) or with the 2D standard culture condition, for both cell lines (figure 4(d)).

3.4. The addition of HA-Nc 0.1% w/v in the matrix enhanced the formation of the 3D Oc dendritic network

To further mimic the bone mineral component in our model (osteomimicry), and provide (i) a surface to which cells can adhere (nano- and micro- scale morphological cues) and (ii) mechanical cues, we added stoichiometric HA-Nc at different concentrations to the matrix blend. We first analysed the distribution and the tendency to form clusters of the HA-Nc in the matrix, also when HA-Nc were dispersed within the matrix outside a microfluidic device, by FEG-SEM (supplementary figure 5). Particles formed aggregates in sparse clusters, which increased in size as HA-Nc concentration increased, reaching a maximum size of 2–4 μ m in diameter at the highest concentrations (0.4% w/v and 0.8% w/v).

To assess the characteristics of the HA-Nc-enriched matrix and its behaviour when co-injected with Oc cell body-sized objects in the microfluidic channel, we used fluorescent microspheres as previously described. The higher the concentrations of HA-Nc, the lower the degradation of the matrix, as evident from the observation of matrix meniscus over time (figure 5(a)). However, the addition of HA-Nc at 0.2, 0.4 and 0.8% w/v led to a less homogeneous distribution of the microspheres along the z-axis (figure 5(b)). From a rheological standpoint, the presence of HA-Nc 0.1% w/v in the Matrigel 75% sample appeared to have no effect on the Amplitude Sweep test, the Frequency sweep test, or the viscosity curve at the two tested temperatures (supplementary figure 6). Nonetheless, at 4 °C, the presence of HA-Nc resulted in a wider IVER, indicating greater stability to deformation stress.

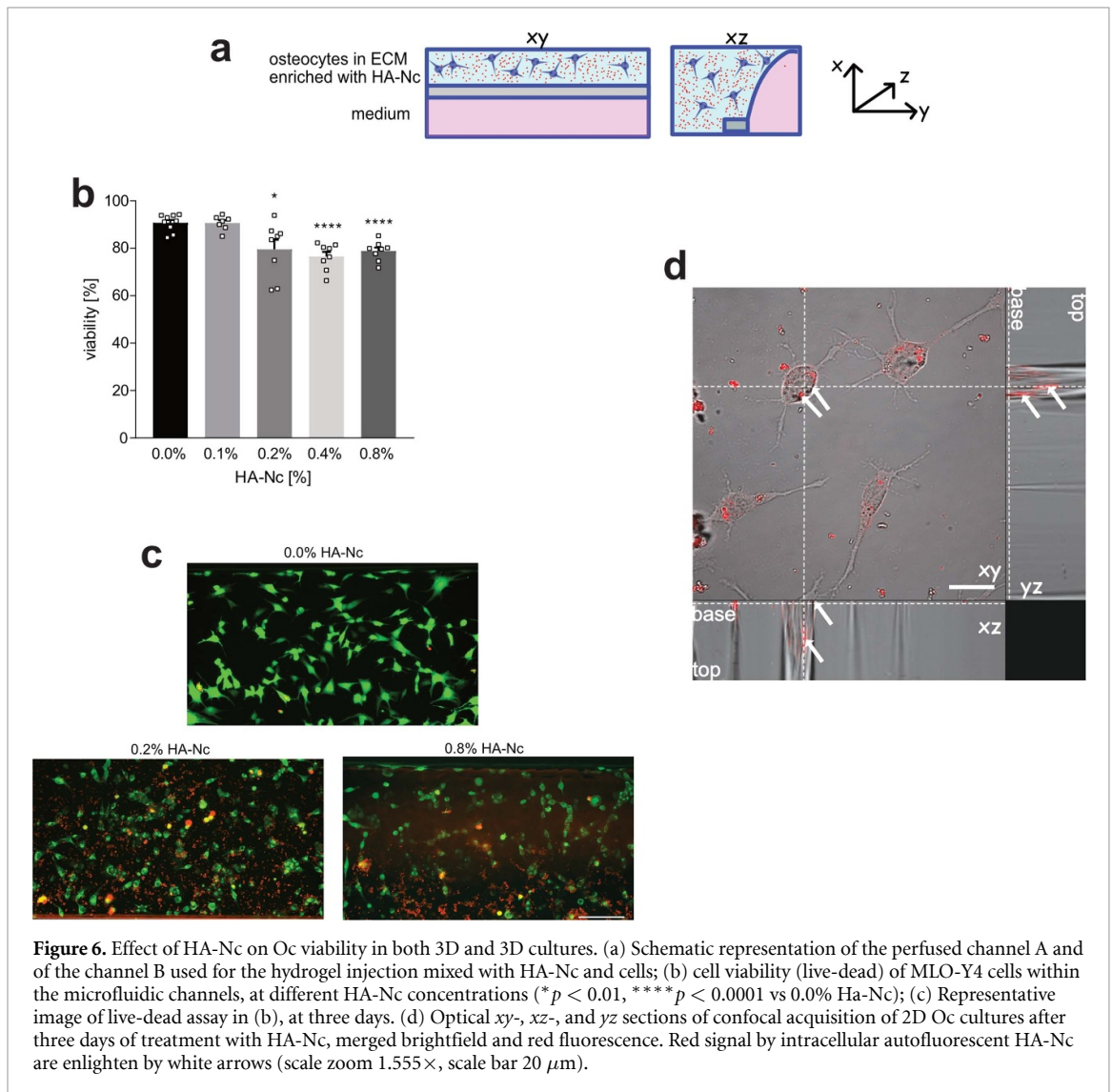
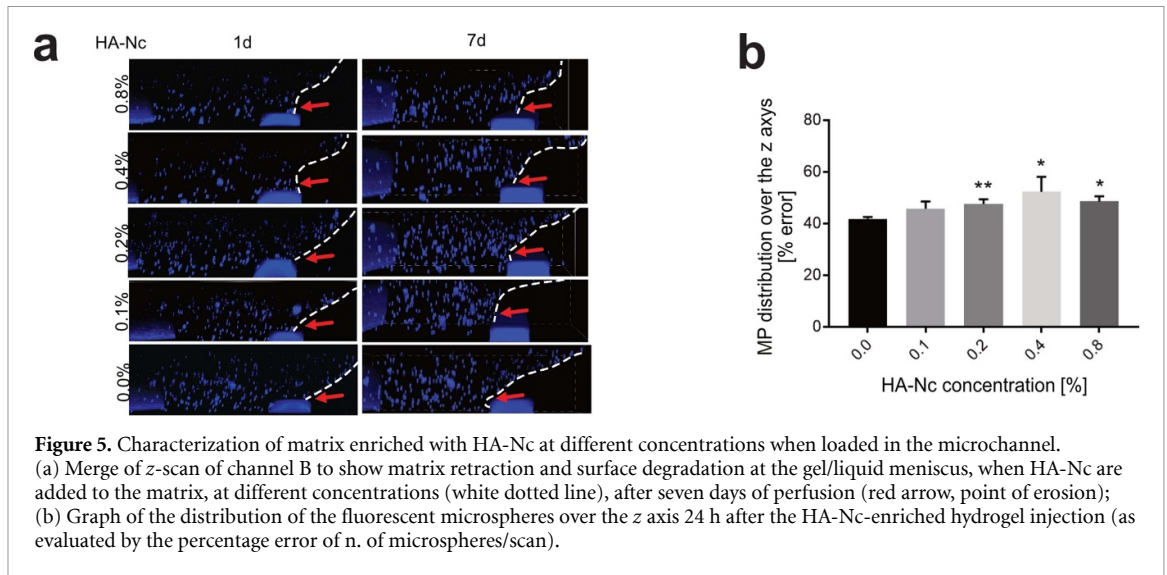
We then combined the HA-Nc-enriched matrix with live Oc (figure 6(a)) and assessed the viability of Oc by the live-dead assay (figures 6(b) and (c), and supplementary figure 7(a)). We found that HA-Nc was cytotoxic for Oc in a dose-dependent manner (figure 6 b and supplementary figure 7(b)). However, at 0.1% w/v HA-Nc, Oc viability after three days of culture was unchanged compared to that of Oc cultures in the absence of HA-Nc (median 81.3% vs 87.4%, respectively, $p = 0.0803$). At the lowest concentration of HA-Nc (0.1% w/v), Oc morphology was unaffected at FEG-SEM observation, whereas at 0.8% w/v concentrations, cells showed a more globular morphology and HA-Nc appeared inside the cells, as confirmed by using 2D cultures and confocal microscopy (figures 6(d) and (e) and supplementary figure 8). In FEG-SEM analysis cell membrane



damage was also visible at the highest concentrations (supplementary figure 8).

Based on these preliminary data, we decided to use HA-Nc only at 0.1% w/v. We performed the same assays to evaluate the induction of Oc differentiation that we used in figure 4, to compare HA-Nc-enriched microfluidic cultures vs microfluidic cultures w/o HA-Nc. From our analysis, we observed that the addition of HA-Nc to the matrix induced a higher ALP (figure 7(a)), whereas the expression and localization of Cx43 were unchanged, both at protein (by immunofluorescence, figure 7(b)) and mRNA levels (figure 7(c)).

mRNA expression of Sost also did not change significantly, although we observed a trend of red). On the contrary, interconnected network between dendritic cells was significantly increased in the HA-Nc-enriched matrix. In order to observe and quantify the formation of dendrite and networks in the 3D Oc cultures, we fixed the cells at three days and immunostained for non-structured β-actin, combined with confocal microscopy to allow the quantification of the length of the cellular network formed by dendrites and cell bodies in the *xyz*-axis (figure 7(d)), within the microchannel B (figure 7(e) and supplementary figures 9 and 10). Automatic quantification showed



that HA-Nc embedded in the matrix promoted dendrite development, but only at a 0.1% w/v (figure 7(f)). It is worth noting that when quantifying the colocalization (Pearson's coefficient), of the signals of

F-actin and integrin alfa-V (CD51), at the confocal microscope, which serve as markers for the formation of focal adhesion structures [51], we observed a slight increase in the trend for the conditions at 0.1%

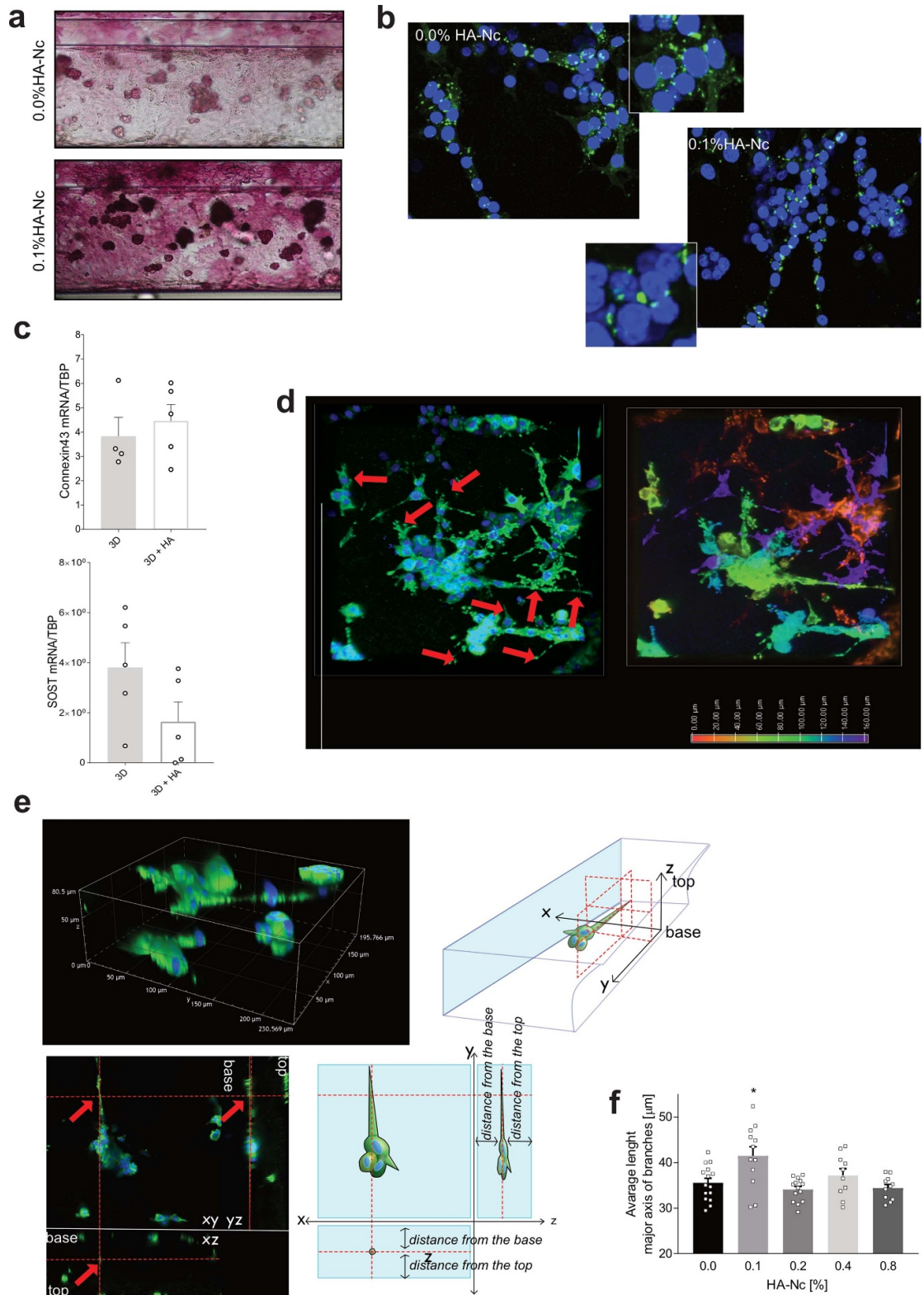


Figure 7. The osteomimetic matrix with NP-HA 0.1% w/v promoted the formation of the dendritic network in the 3D microfluidic Oc cultures. (a) Alkaline phosphatase staining of Oc cultured in the osteomimetic matrix (with HA-Nc at 0.1% w/v), in perfused condition in respect to Oc cultured in the collagenic matrix mix, without HA-Nc. Representative images of channel B of one chip in the microfluidic plate (objective 20×). (b) Representative images of the fixed Oc cultured within the osteomimetic matrix (with HA-Nc at 0.1% w/v) or in the collagenic matrix without HA-Nc, in perfused condition. Cells were then immunostained for Cx43 (green), counterstained with Hoechst 33258 (blue), and observed by confocal microscopy (merge of 86 xy sections, z-step of 2 μm, objective 20×, NA 0.75). In the square, a higher magnification of the same field. (c) mRNA analysis by Q-RT-PCR of Cx43 and sclerostin (Sost) of Oc cultured for three days in the microfluidic chip in passive perfused condition, within the osteomimetic matrix or in the matrix w/o HA-Nc. (d) Representative merged images of the dendritic network of Oc cultured within the osteomimetic matrix (HA-Nc 0.1% w/v), after fixation and immunostaining for G-actin (green) and counterstained with Hoechst 33258 (blue). False colour image for the Z-axis. (e) Representative volume render reconstruction of a single dendrite protruded in the 3D space. A single xyz scan is also shown; (f) Graph on the average length of dendrites of the Oc 3D cultures within the osteomimetic matrix, at different HA-Nc concentrations, after the automatic quantification of the confocal scan with NIS-Element software (*p < 0.05).

w/v Ha-Nc and a significant decrease at 0.2% w/v Ha-Nc (supplementary figure 11, Pearson). These results also partially reflect the trend observed in the viability assay (figure 6(b))

3.5. Validation of the 3D model of the perfused dendritic network as a platform for the screening of Oc-targeted drugs

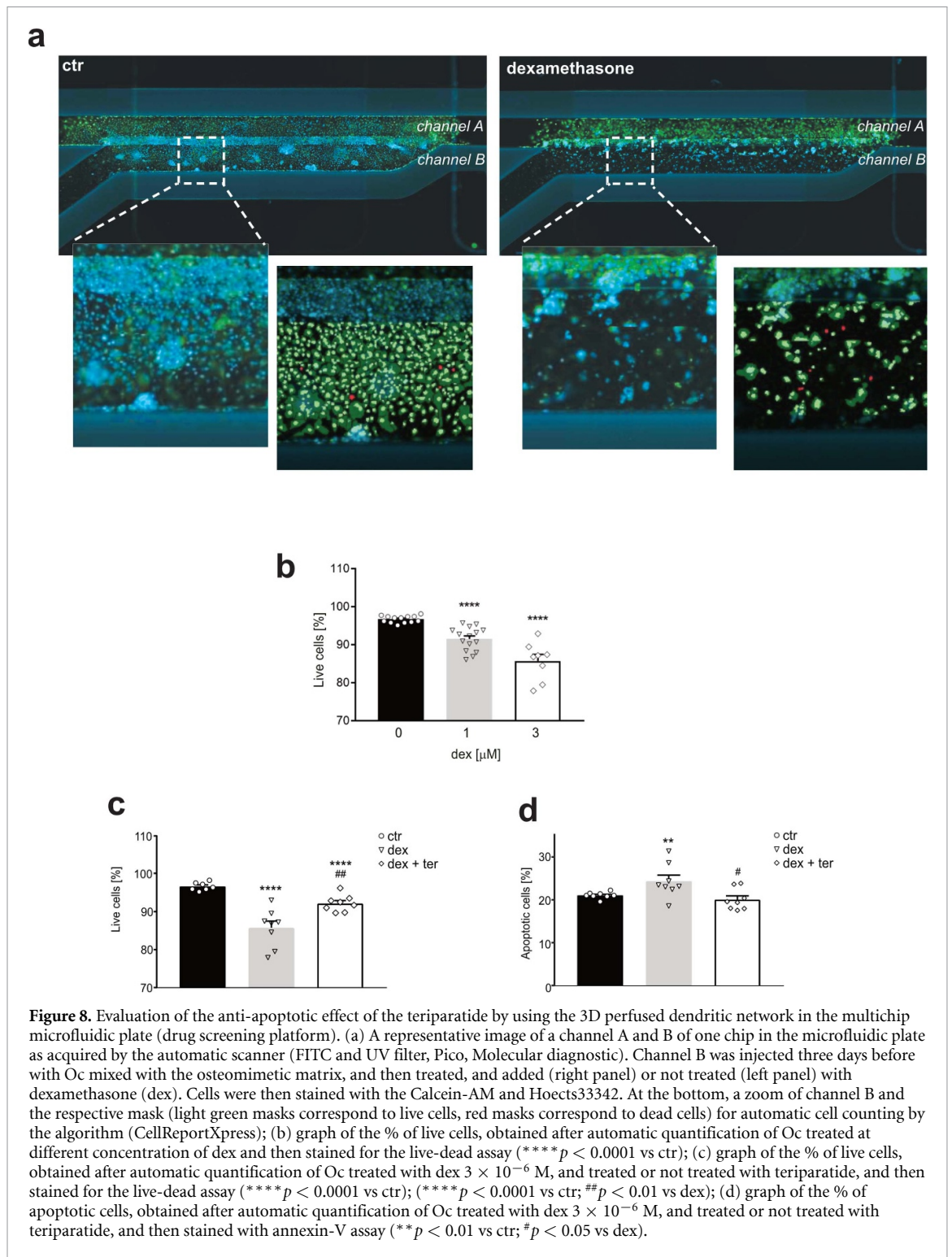
To test whether the 3D Oc *in vitro* model is a valuable model to screen Oc-targeting therapeutics, we used a teriparatide, a drug that is currently used to treat osteoporosis and that has anti-apoptotic effects on Oc stressed by glucocorticoids [18]. For this purpose, we both counted live cells and performed an apoptosis assay. Both assays were acquired and analysed by an automatic scanner compatible with microfluidic 96-chip plates. This system quantifies and automatically analyses the fluorescent signals within the entire depth of the chip (figure 8(a)). As a first step, we confirmed that dexamethasone (dex), used as glucocorticoid, was able to induce cell death in a dose-dependent manner (figure 8(b)). The use of a multichip platform allowed a very highly reproducible result for this assay (dex 1 μM vs ctr, **** $p < 0.0001$). We then choose the 3 μM concentration to combine with teriparatide (ter, 300 nM), and found that teriparatide significantly reduced the cytotoxic effect of dexamethasone in Oc, as expected (figure 8(c)). Again, results were obtained with a high degree of reproducibility (dex + ter vs dex alone, ## $p = 0.0023$). Finally, the annexin-V assay data were in agreement with those obtained with the live-dead assay, albeit with a higher degree of variability (figure 8(d), dex + ter vs dex alone, # $p = 0.049$).

4. Discussion

The deeply interconnected Oc network is becoming an important pharmaceutical target for the treatment of various bone-related diseases. Therefore, the development of adequate preclinical models that can mimic the very complex cellularized structure of the Oc network is an important pharmaceutical target for the treatment of bone diseases. Therefore, the development of adequate preclinical models that can mimic the complex structure of the Oc network is of great interest. To mimic the real setting of bone tissue, 3D Oc culture must be combined osteomimetic ECM, dynamic perfusion, and mechanical cues (i.e., shear stress). There are only very few examples of 3D models of Oc, which highlights the complexity of this type of culture, but also its novelty. In these examples, hydrogels, inorganic biomaterials, or dynamic stimulation, have been used without consideration to the combination of these elements in a single complex model [24–33]. To fill this gap, we used a microfluidic device that reproduced the fine

cell-cell and cell-ECM communication of Oc and in which shear stress can be applied. In addition, the small size of the microchannels (330 μm in width and 220 μm in height) also facilitates the real-time visualization and the monitoring of the living Oc 3D network within the gel over time. Finally, miniaturisation of the model and the development of multiple Oc networks in the same platform pave the way for large-scale drug screening [52].

To build the model, we proceeded stepwise. First, we selected the most suitable biomaterial for Oc in gel culture within microfluidic channels. Although several types of hydrogels are available for macroscale models [53], to date, there is a lack of standards for microfluidics. This is possibly a consequence of the limitation of this technology, which almost exclusively allows the injection of reverse thermoresponsive hydrogels whose sol-gel transition temperature is above 20 °C [54–56] to be handled, and under 37 °C not to harm cells. The use of chemical crosslinking agents is not possible as they should be added after loading of the cell-enriched gel into the microfluidic channel but they are cytotoxic. The most widely used hydrogel for Oc cultures is rat tail Type I collagen, which closely resembles the organic component of the bone tissue. However, the fine-tuning of collagen scaffold properties *in vitro* is not on par with the properties observed *in vivo* tissues [57]. As stated in the literature, the primary limitation of using collagen for engineered collagen scaffolds (i.e., 3D structured gels) is its inadequate mechanical strength, low compressive strength and stiffness, poor structural stability, and rapid degradation [57–59]. Consequently, collagen is mostly considered for 2D surface coatings rather than as an ECM for 3D tissue models or, in some cases, as filler of other biomaterials as a non-structural component, to enhance cell adhesion, proliferation, and migration [60]. The main reason for these limitations is the relatively low concentrations (<10 mg ml⁻¹) of rat tail type I collagen solutions, which significantly restrict their applications [58]. Lower concentrations lead to reduced viscosity and, consequently, hinder the gel preparation process. One potential solution is to increase the collagen concentration in the initial solution for 3D applications in *in vitro* models. In this study, we tried to use highly concentrated collagenic matrix (Cultrex™ 3D Culture Matrix™) as a scaffold and, as a first step, we compared it to Matrigel®, in terms of stability and shape retention in microfluidic channels, under continuous perfusion. We chose Matrigel® for our experiments because, despite its complex, ill-defined, and variable composition, and poor reproducibility, it is one of the few reverse thermoresponsive injectable hydrogels that can be successfully loaded into a microfluidic channel. Moreover, it is still one of the most commonly used hydrogels for cell culture due to



its availability, ease of use, and versatility for culturing different types of cells. Matrigel® has been widely used, including recently, in 3D experiments in cell biology to reproduce *in vivo* conditions for both normal and pathological states [61–65]. Matrigel® is a highly bioactive gel matrix that contains variable and uncontrollable concentrations of several matrix proteins (e.g. laminin, collagen IV, and enactin) [66] and soluble growth factors (e.g. fibroblast growth factor

and epidermal growth factor) [65]. Furthermore, despite its extensive use in 3D modelling, Matrigel® has not yet been explored for Oc culture.

Physical properties (e.g. volume changes) of an hydrogel largely depends on the degree of confinement and the geometry of the confined region [67], and evaluate its physical properties outside the microchannel would have not been informative. However, to date, there are no ways to characterize

a hydrogel when it is inside a microchannel. Thus, we performed rheological tests on the hydrogels used, and as expected, we found an elastic modulus between 10 and 100 Pa (supplementary figure 2(d)) which is considerably lower than the elastic module of human bone (3–20 GPa). Therefore, we choose the hydrogel and the collagen concentrations based on the best solution that allowed for gel loading in the microfluidic device without exerting high shear stress on the cells during the loading, ensuring homogeneous cell distribution within the gel and an appropriate cell viability over time, without considering the elastic modulus.

We thus developed an ad hoc protocol based on fluorescence microbeads. We dispersed a high-density suspension of cells-sized fluorescent microbeads in the gels and monitored their distribution over time. We observed that Cultrex™ was less prone to shear stress-induced surface degradation than Matrigel®. However, Cultrex™ showed a greater tendency to shrink and detach from the wall of the microfluidic channel in which it was injected. This may be due to the higher stiffness of high concentration Cultrex™ compared to Matrigel®: the higher the stiffness, the lower the mass loss when the hydrogel is subjected to mechanical stimuli [68]. Also, compared with Matrigel®, when added to Cultrex™, the microbeads were less homogeneously dispersed along the thickness of the gel, increasing the risk of cluster formation. An increase in collagen concentration may lead to an increase in fibre density and a reduction in the hydrogel pore size which could hinder microbeads dispersion [69]. The formation of cell cluster may prevent Oc to distribute within the gel at distances similar to those *in vivo*, which is instead essential to allow the formation of dendrites [31]. Thus, in our study, Cultrex™ was dismissed. However, we decided to use a liquid, low-concentration, collagen solution as a filler of Matrigel® to further enrich with Type I collagen the hydrogel since it is richly present in bone. Liquid collagen has been already used as a filler of Matrigel®, but also of alginate, GelMA, and chitosan [60, 70–73]. The observations made through microscopy were confirmed by rheological analysis of the gels. At 4 °C, Cultrex™ exhibited a ‘solid-like’ behaviour and was stiffer and characterized by higher viscosity than Matrigel samples, requiring more force to deform it. This characteristic of Cultrex™ was linked to the difficulty to uniformly mix the fluorescent microparticles within the gel and could potentially affect cell viability during loading into the microfluidic device. At 37 °C, the distinction between the gels narrowed, possibly due to the thermal cross-linking of Matrigel, enhancing its mechanical stability and stiffness. When comparing 90% matrigel and 75% matrigel, the operator-perceived difficulty in the

gel loading into the microfluidic channels with 90% matrigel is confirmed by viscosity analysis.

Next, we evaluated the viability and differentiation of Oc embedded within the Matrigel®/collagen blend. MLO-Y4 cells showed higher viability than MLO-A5. As Oc-like cells, MLO-Y4 has a lower proliferation rate than the osteoblasts which could result in less matrix degradation and nutrient consumption [74]. Furthermore, *in vivo*, under physiological conditions, Oc reside in interconnected microscopic spaces and are surrounded by a stiff ECM, whereas, in growing bone, osteoblasts are not surrounded by calcified bone matrix, but are located on the surface of soft osteoid in highly porous regions [75–77]. Therefore, it is likely that MLO-Y4 survive better than MLO-A5 in matrices with high stiffness, such as those obtained with the hydrogel blend [34]. We next studied Oc differentiation within the chip by analysing cell morphology and the expression of Oc markers as Cx43 and ALP. Based on literature, Oc differentiation is significantly enhanced when cultured in 3D. As a confirmation, in our model, Cx43 was more highly expressed in 3D than 2D, in both in Oc and in Ob-like models, but in MLO-Y4 were higher and redistributed at the contact point between the cells. In the 3D dynamic culture conditions, Oc also highly expressed the other focal adhesion markers (integrin alphaV/CD51). This suggests an increased differentiation and the establishment of a true cellular network. Cx43 is the major gap junction expressed in Oc to form and regulate a functional ‘3D syncytium’ that connects different cells throughout the bone. In Oc, Cx43-dependent gap junctions and hemichannels contribute to the coordination of bone remodelling in response to anabolic factors and mechanical loading [78]. It is worth to mention that FSS stimuli regulate Cx43 expression [79]. Similarly, we found significantly higher expression of Sost, a very important Oc-derived glycoprotein which regulate the osteoblast-osteoclast coupling. We also noticed that within the microfluidic chip, when adherent to a 2D hard surface subjected to shear-stress, as in channel A, MLO-Y4 cells reorganized actin into stress fibres. In contrast, when embedded in the matrix blend, the stress fibres disappear and focal adhesions redistribute, both at the periphery and at the cell body, as opposed to 2D conditions in which focal adhesions are more localized to the periphery [80]. Focal adhesion are macromolecular complexes of proteins that serve as physical linkage between cytoskeleton and the ECM and in Oc are particularly crucial for mechanotransduction [81]. When entrapped in lacunae in bone, Oc, at the interface between collagen hillocks and dendrites, express integrin-mediated focal adhesions that connect the cell membrane with the ECM and transmit physical signals to the cytoskeleton [80]. We then

explored the osteoblast-related marker ALP that, as expected, was lower than in MLO-A5.

Having confirmed that the miniaturized microfluidic model is suitable to culture Oc and maintain their differentiation, we took a step forward towards a higher level of osteomimicry by dispersing an inorganic phase in the organic matrix. It is difficult to fully reproduce native bone apatite *in vitro*. Several types of calcium phosphate (CaP)-based bone substitutes have been explored in the literature [82]. We used HA-Nc because HA is natural mineral and component of the bone, comprising about 50% of the bone weight [83], and is highly bioactive and biocompatible, and mimics well the mineral composition of bone in vertebrates. In fact, compared with other calcium phosphate-based bio-ceramics, such as TCP, HA is more stable and less soluble at body temperature, with a stoichiometric Ca/P ratio of 1.67, very similar to that of bone [84, 85]. Nanosized HA has been used as reinforcement of nanocomposite hydrogel scaffolds designed for bone tissue engineering and, when embedded into a collagen-based matrix, buttresses the nanocomposite structure by increasing its compressive strength and creating bioactive sites for protein adhesion, thereby improving cell attachment [86]. In this case, we used nanosized HA to not affect the injectability of the matrix blend into the microchannel and to improve matrix stiffness. We dispersed Ncs of HA, synthesized as described previously [45, 46], in the Matrigel[®]/collagen blend and evaluated their effects on gel stability and on Oc viability. The extent of degradation of the hydrogel surface at the meniscus increased inversely with respect to the concentration of Ha-Nc. As mentioned before, this type of filler induces compactness. However, increasing the percentage of HA-Nc resulted in a lower distribution of cell-sized objects within the hydrogel and an increased the formation of HA-Nc clusters. This could be due to the protocol for the preparation of the final injectable composite hydrogel: not to harm the physical and biological properties of Matrigel[®], the mixture with HA-Nc was sonicated only before its mixing with matrix blend. The formation of HA-Nc clusters at the highest HA-Nc concentrations has been confirmed also by SEM analysis. The co-presence of nano- and micro-sized particles may advantageously result in higher material viscosity, stiffness, and shear stress [87]. However, at the highest doses, HA-Nc induced Oc toxicity in a dose-dependent manner that was likely caused by the uptake of Ncs from cells, as revealed by the autofluorescence signal of HA-Nc clusters and by ultrastructural analysis. The uptake of HA-Nc is consistent with previous reports showing that HA can be phagocytosed by Oc [88]. Vice versa, the lowest concentration of HA-Nc was not cytotoxic and, most

importantly, promoted dendrite formation, suggesting the formation of HA-Nc-induced podosomes at the cell-material interphase [89]. Therefore, we set 0.1% w/v HA-Nc concentration for our osteomimetic matrix.

In order to validate the 3D dendritic network obtained within the microchip as a screening platform for Oc-targeted pharmaceutical approaches, we then evaluated the effectiveness of a very common anabolic drug for the treatment of osteoporosis, teriparatide. Osteoporosis is a progressive chronic disease of bone metabolism, characterized by decreased bone mass and mineral density and deterioration of bone architecture, which predisposes individuals to an increased risk of fractures. One of the most frequent causative factor is the decline in oestrogen levels, as it occurs during menopause [90]. Among the several effects on bone, oestrogen protect cells of the osteogenic lineage, including Oc, from apoptosis and senescence [91]. To mimic the osteoporotic phenotype *in vitro*, we treated Oc with a glucocorticoid, dexamethasone, that is oestrogen antagonist [92] and that induces Oc apoptosis [14]. As expected, in our platform, teriparatide treatment successfully promoted the viability of dexamethasone-pre-treated Oc in a highly reproducible fashion, by reducing their apoptosis.

Overall, the Mimetas two-lane OrganoPlate[®] device was well-suited to develop a 3D network of Oc to mimic osteoporosis and validate the model with teriparatide. This is the first time that the device has been used to build a bone tissue model, thanks to (i) the possibility to modulate gel composition, (ii) the channels' geometry, (iii) the absence of artificial membranes enabling culture medium diffusion and exchange of factors, and (iv) the possibility to perform multiple in-plate and off-plate assays. Additionally, the high number of chips in the device makes it suitable for high-throughput screening. However, despite the device's several advantages, there are some limitations in its use. The major limitation is that the microfluidic device is disposable and non-openable, with limited possibilities for creating channel coatings. This closed and non-openable system makes the cell extraction process for RNA isolation and Q-RT-PCR difficult and time-consuming. Additionally, it is not feasible to analyse the cell-loaded gel in the channel using an environmental scanning electron microscope to gain a more comprehensive understanding of the interactions between cell-matrix and cell-nanohydroxyapatite, as well as the porosity of the gel. While it is essential to assess the porosity of the ECM and ensure that it closely resembles the characteristics of the *in vivo* ECM for developing a new *in vitro* bone model, this study was unable to perform such an analysis due to technical limitations of the

device technology. Further advancements in characterisation techniques and protocols will be necessary to address and resolve this critical gap.

5. Conclusions

Overall, we have engineered a commercial microfluidic device that has never been used for orthopaedic research and that enables the development of a 3D Oc network. To date, 3D models of Oc are very scarce, and in any case, they do not include both the matrix and the mineral part of bone in addition to shear stress, all of which are critical for the expression of Oc phenotype. We created a mixture of collagen-enriched blend, added with HA-Nc for osteomimicry that could be successfully mixed with cells and injected into a channel of the commercial microfluidic device. The combined use of the developed osteomimetic matrix and the microfluidic device was found to be highly permissive for formation of Oc networks, similar to those *in vivo*, and highly reproducible. After being extensively characterized for Oc viability and differentiation, the device was found to be suitable for large-scale screening of bone anabolic drugs. Indeed, Oc are a major target for the treatment of osteoporosis and other Oc-related diseases. In the future, this platform has the potential to speed up the development of new treatments and personalised approaches, as it is suitable for a very small number of cells, such as the patient-derived Oc progenitors.

Data availability statement

The data cannot be made publicly available upon publication because they are not available in a format that is sufficiently accessible or reusable by other researchers. The data that support the findings of this study are available upon reasonable request from the authors.

Acknowledgments

The work was supported by Italian Association for Cancer Research (AIRC IG 2021—ID 25749 to SA) and by Italian Ministry of Health ('Progetti di ricerca per metodi alternativi alla sperimentazione animale' art. 41 c. 2 del d.lgs. 26/2014 for 2021 to SA), and by Italian Ministry of Health (5 × 1000 Anno 2020, Redditi 2019 'Prevenzione, diagnosi e trattamento della fragilità ossea' to NB), and by MUR-M4C2 1.3 of National Recovery and Resilience Plan PNRR, PE8-AGE-IT (PE0000015 to NB).

ORCID iDs

Elisa Boanini  <https://orcid.org/0000-0003-3754-0273>

Sofia Avnet  <https://orcid.org/0000-0002-7843-0591>

References

- [1] Bonewald L F 2011 The amazing osteocyte *J. Bone Miner. Res.* **26** 229–38
- [2] Bonewald L F 2017 The role of the osteocyte in bone and nonbone disease *Endocrinol. Metab. Clin. North Am.* **46** 1–18
- [3] Buenzli P R and Sims N A 2015 Quantifying the osteocyte network in the human skeleton *Bone* **75** 144–50
- [4] Delgado-Calle J and Bellido T 2022 The osteocyte as a signaling cell *Physiol. Rev.* **102** 379–410
- [5] Uda Y, Azab E, Sun N, Shi C and Pajevic P D 2017 Osteocyte mechanobiology *Curr. Osteoporos. Rep.* **15** 318–25
- [6] Robling A G and Bonewald L F 2020 The osteocyte: new insights *Annu. Rev. Physiol.* **82** 485–506
- [7] Dallas S L, Prideaux M and Bonewald L F 2013 The osteocyte: an endocrine cell and more *Endocr. Rev.* **34** 658–90
- [8] Metzger C E and Narayanan S A 2019 The role of osteocytes in inflammatory bone loss *Front. Endocrinol.* **10** 285
- [9] Choi J U A, Kijas A W, Lauko J and Rowan A E 2021 The mechanosensory role of osteocytes and implications for bone health and disease states *Front. Cell Dev. Biol.* **9** 770143
- [10] ten Dijke P, Krause C, de Gorter D J, Lowik C W and van Bezooijen R L 2008 Osteocyte-derived sclerostin inhibits bone formation: its role in bone morphogenetic protein and Wnt signaling *J. Bone Joint Surg. Am.* **90** 31–35
- [11] Ru J Y and Wang Y F 2020 Osteocyte apoptosis: the roles and key molecular mechanisms in resorption-related bone diseases *Cell Death Dis.* **11** 846
- [12] Manolagas S C and Parfitt A M 2013 For whom the bell tolls: distress signals from long-lived osteocytes and the pathogenesis of metabolic bone diseases *Bone* **54** 272–8
- [13] Pathak J L, Bravenboer N and Klein-Nulend J 2020 The osteocyte as the new discovery of therapeutic options in rare bone diseases *Front. Endocrinol.* **11** 405
- [14] Jilka R L, Noble B and Weinstein R S 2013 Osteocyte apoptosis *Bone* **54** 264–71
- [15] Kaur J, Khosla S and Farr J N 2022 Effects of diabetes on osteocytes *Curr. Opin. Endocrinol. Diabetes Obes.* **29** 310–7
- [16] Pin F, Prideaux M, Bonewald L F and Bonetto A 2021 Osteocytes and cancer *Curr. Osteoporos. Rep.* **19** 616–25
- [17] Poutoglidou F, Samoladas E, Raikos N and Kouvelas D 2021 Efficacy and safety of anti-sclerostin antibodies in the treatment of osteoporosis: a meta-analysis and systematic review *J. Clin. Densitom.* **25** 401–15
- [18] Wang T, Han C, Tian P, Li P F and Ma X L 2018 Role of teriparatide in glucocorticoid-induced osteoporosis through regulating cellular reactive oxygen species *Orthop. Surg.* **10** 152–9
- [19] Smargiassi A et al 2020 WISP-2 expression induced by Teriparatide treatment affects *in vitro* osteoblast differentiation and improves *in vivo* osteogenesis *Mol. Cell. Endocrinol.* **513** 110817
- [20] Gatti D, Rossini M, Viapiana O, Povino M R, Liuzza S, Fracassi E, Idolazzi L and Adami S 2013 Teriparatide treatment in adult patients with osteogenesis imperfecta type I *Calcif. Tissue Int.* **93** 448–52
- [21] Hoyer-Kuhn H, Semler O, Stark C, Struebing N, Goebel O and Schoenau E 2014 A specialized rehabilitation approach improves mobility in children with osteogenesis imperfecta *J. Musculoskelet. Neuronal Interact.* **14** 445–53
- [22] Ralston S H and Gaston M S 2019 Management of osteogenesis imperfecta *Front. Endocrinol.* **10** 924
- [23] Wang Y and Jeon H 2022 3D cell cultures toward quantitative high-throughput drug screening *Trends Pharmacol. Sci.* **43** 569–81
- [24] Aziz A H, Wilmoth R L, Ferguson V L and Bryant S J 2020 IDG-SW3 osteocyte differentiation and bone extracellular matrix deposition are enhanced in a 3D matrix

- metalloproteinase-sensitive hydrogel *ACS Appl. Biol. Mater.* **3** 1666–80
- [25] Mc Garrigle M J, Mullen C A, Haugh M G, Voisin M C and McNamara L M 2016 Osteocyte differentiation and the formation of an interconnected cellular network *in vitro Eur. Cell Mater.* **31** 323–40
- [26] Kurata K, Heino T J, Higaki H and Vaananen H K 2006 Bone marrow cell differentiation induced by mechanically damaged osteocytes in 3D gel-embedded culture *J. Bone Miner. Res.* **21** 616–25
- [27] Yang Y, Wang M, Yang S, Lin Y, Zhou Q, Li H and Tang T 2020 Bioprinting of an osteocyte network for biomimetic mineralization *Biofabrication* **12** 045013
- [28] Matsugaki A, Matsuzaka T, Murakami A, Wang P and Nakano T 2020 3D printing of anisotropic bone-mimetic structure with controlled fluid flow stimuli for osteocytes: flow orientation determines the elongation of dendrites *Int. J. Bioprint.* **6** 293
- [29] Bernhardt A, Skottke J, von Witzleben M and Gelinsky M 2021 Triple culture of primary human osteoblasts, osteoclasts and osteocytes as an *in vitro* bone model *Int. J. Mol. Sci.* **22** 7316
- [30] Boukhechba F, Balaguer T, Michiels J F, Ackermann K, Quincey D, Boulter J M, Pyerin W, Carle G F and Rochet N 2009 Human primary osteocyte differentiation in a 3D culture system *J. Bone Miner. Res.* **24** 1927–35
- [31] Sun Q, Choudhary S, Mannion C, Kissin Y, Zilberberg J and Lee W Y 2018 Ex vivo replication of phenotypic functions of osteocytes through biomimetic 3D bone tissue construction *Bone* **106** 148–55
- [32] Choudhary S, Sun Q, Mannion C, Kissin Y, Zilberberg J and Lee W Y 2018 Hypoxic three-dimensional cellular network construction replicates ex vivo the phenotype of primary human osteocytes *Tissue Eng. A* **24** 458–68
- [33] Sun Q, Gu Y, Zhang W, Dziopa L, Zilberberg J and Lee W 2015 Ex vivo 3D osteocyte network construction with primary murine bone cells *Bone Res.* **3** 15026
- [34] Lipreri M V, Baldini N, Graziani G and Avnet S 2021 Perfused platforms to mimic bone microenvironment at the macro/milli/microscale: pros and cons *Front. Cell Dev. Biol.* **9** 760667
- [35] Komori T 2015 Animal models for osteoporosis *Eur. J. Pharmacol.* **759** 287–94
- [36] Haffner-Luntzer M, Hankenson K D, Ignatius A, Pfeifer R, Khader B A, Hildebrand F, Griensven M, Pape H-C and Lehmiche M 2019 Review of animal models of comorbidities in fracture-healing research *J. Orthop. Res.* **37** 2491–8
- [37] Sandha K K, Shukla M K and Gupta P N 2020 Recent advances in strategies for extracellular matrix degradation and synthesis inhibition for improved therapy of solid tumors *Curr. Pharm. Des.* **26** 5456–67
- [38] Barbosa M A G, Xavier C P R, Pereira R F, Petrikaite V and Vasconcelos M H 2021 3D cell culture models as recapitulators of the tumor microenvironment for the screening of anti-cancer drugs *Cancers* **14** 190
- [39] Jiang Y, Zhang H, Wang J, Liu Y, Luo T and Hua H 2022 Targeting extracellular matrix stiffness and mechanotransducers to improve cancer therapy *J. Hematol. Oncol.* **15** 34
- [40] Robin M, Almeida C, Azais T, Haye B, Illoul C, Lesieur J, Giraud-Guille -M-M, Nassif N and H elary C 2016 Involvement of 3D osteoblast migration and bone apatite during *in vitro* early osteocytogenesis *Bone* **88** 146–56
- [41] Akther F, Little P, Li Z, Nguyen N T and Ta H T 2020 Hydrogels as artificial matrices for cell seeding in microfluidic devices *RSC Adv.* **10** 43682–703
- [42] Vriend J et al 2020 Flow stimulates drug transport in a human kidney proximal tubule-on-a-chip independent of primary cilia *Biochim. Biophys. Acta Gen. Subj.* **1864** 129433
- [43] Vulto P, Podszun S, Meyer P, Hermann C, Manz A and Urban G A 2011 Phaseguides: a paradigm shift in microfluidic priming and emptying *Lab Chip* **11** 1596–602
- [44] Cheng B, Zhao S, Luo J, Sprague E, Bonewald L F and Jiang J X 2001 Expression of functional gap junctions and regulation by fluid flow in osteocyte-like MLO-Y4 cells *J. Bone Miner. Res.* **16** 249–59
- [45] Pezzatini S, Morbidelli L, Solito R, Paccagnini E, Boanini E, Bigi A and Ziche M 2007 Nanostructured HA crystals up-regulate FGF-2 expression and activity in microvascular endothelium promoting angiogenesis *Bone* **41** 523–34
- [46] Boanini E, Torricelli P, Cassani M C, Rubini K, Fini M, Pagani S and Bigi A 2020 Platinum nanoparticles supported on functionalized hydroxyapatite: anti-oxidant properties and bone cells response *Ceram Int.* **46** 19574–82
- [47] Kato Y, Windle J J, Koop B A, Mundy G R and Bonewald L F 1997 Establishment of an osteocyte-like cell line, MLO-Y4 *J. Bone Miner. Res.* **12** 2014–23
- [48] Kato Y, Boskey A, Spevak L, Dallas M, Hori M and Bonewald L F 2001 Establishment of an osteoid preosteocyte-like cell MLO-A5 that spontaneously mineralizes in culture *J. Bone Miner. Res.* **16** 1622–33
- [49] Tanaka-Kamioka K, Kamioka H, Ris H and Lim S S 1998 Osteocyte shape is dependent on actin filaments and osteocyte processes are unique actin-rich projections *J. Bone Miner. Res.* **13** 1555–68
- [50] Brady R T, O'Brien F J and Hoey D A 2022 The impact of the extracellular matrix environment on sost expression by the MLO-Y4 osteocyte cell line *Bioengineering* **9** 35
- [51] Ivaska J 2012 Unanchoring integrins in focal adhesions *Nat. Cell Biol.* **14** 981–3
- [52] De Stefano P, Bianchi E and Dubini G 2022 The impact of microfluidics in high-throughput drug-screening applications *Biomicrofluidics* **16** 031501
- [53] Yue S, He H, Li B and Hou T 2020 Hydrogel as a biomaterial for bone tissue engineering: a review *Nanomaterials* **10** 1511
- [54] Zhang K, Xue K and Loh X J 2021 Thermo-responsive hydrogels: from recent progress to biomedical applications *Gels* **7** 77
- [55] Rafael D, Melendres M M R, Andrade F, Montero S, Martinez-Trucharte F, Vilar-Hernandez M, Dur n-Lara E F, Schwartz S Jr and Abasolo I 2021 Thermo-responsive hydrogels for cancer local therapy: challenges and state-of-art *Int. J. Pharm.* **606** 120954
- [56] Bonetti L, De Nardo L and Fare S 2021 Thermo-responsive methylcellulose hydrogels: from design to applications as smart biomaterials *Tissue Eng. B* **27** 486–513
- [57] Vaez M, Asgari M, Hirvonen L, Bakir G, Khattignavong E, Ezzo M, Aguayo S, Schuh C M, Gough K and Bozec L 2023 Modulation of the biophysical and biochemical properties of collagen by glycation for tissue engineering applications *Acta Biomater.* **155** 182–98
- [58] Qi P W, Zhou Y Y, Wang D L, He Z H and Li Z J 2015 A new collagen solution with high concentration and collagen native structure perfectly preserved *RSC Adv.* **5** 87180–6
- [59] Rangel A H, Pimentel R G C and Martinez E S 2022 Improvement of mechanical properties of collagen electrospun mats by halloysite nanotubes *J. Mater. Res. Technol.* **20** 3592–9
- [60] Anguiano M et al 2020 The use of mixed collagen-Matrigel matrices of increasing complexity recapitulates the biphasic role of cell adhesion in cancer cell migration: ECM sensing, remodeling and forces at the leading edge of cancer invasion *PLoS One* **15** e0220019
- [61] Drakhlis L, Devadas S B and Zweigerdt R 2021 Generation of heart-forming organoids from human pluripotent stem cells *Nat. Protoc.* **16** 5652–72
- [62] Marchini A and Gelain F 2022 Synthetic scaffolds for 3D cell cultures and organoids: applications in regenerative medicine *Crit. Rev. Biotechnol.* **42** 468–86
- [63] Jose G, Shalumon K T and Chen J P 2020 Natural polymers based hydrogels for cell culture applications *Curr. Med. Chem.* **27** 2734–76
- [64] Kim S et al 2022 Tissue extracellular matrix hydrogels as alternatives to Matrigel for culturing gastrointestinal organoids *Nat. Commun.* **13** 1692

- [65] Aisenbrey E A and Murphy W L 2020 Synthetic alternatives to Matrigel *Nat. Rev. Mater.* **5** 539–51
- [66] Hughes C S, Postovit L M and Lajoie G A 2010 Matrigel: a complex protein mixture required for optimal growth of cell culture *Proteomics* **10** 1886–90
- [67] Li Y, Sariyer O S, Ramachandran A, Panyukov S, Rubinstein M and Kumacheva E 2015 Universal behavior of hydrogels confined to narrow capillaries *Sci. Rep.* **5** 17017
- [68] Dey K, Agnelli S, Borsani E and Sartore L 2021 Degradation-dependent stress relaxing semi-interpenetrating networks of hydroxyethyl cellulose in Gelatin-PEG hydrogel with good mechanical stability and reversibility *Gels* **7** 277
- [69] Habanjar O, Diab-Assaf M, Caldefie-Chezet F and Delort L 2021 3D cell culture systems: tumor application, advantages, and disadvantages *Int. J. Mol. Sci.* **22** 12200
- [70] Moxon S R, Corbett N J, Fisher K, Potjewyd G, Domingos M and Hooper N M 2019 Blended alginate/collagen hydrogels promote neurogenesis and neuronal maturation *Mater. Sci. Eng. C* **104** 109904
- [71] Geanaliu-Nicolae R E and Andronescu E 2020 Blended natural support materials-collagen based hydrogels used in biomedicine *Materials* **13** 5641
- [72] Stratsteffen H, Kopf M, Kreimendahl F, Blaeser A, Jockenhoevel S and Fischer H 2017 GelMA-collagen blends enable drop-on-demand 3D printability and promote angiogenesis *Biofabrication* **9** 045002
- [73] Reis L A, Chiu L L, Liang Y, Hyunh K, Momen A and Radisic M 2012 A peptide-modified chitosan-collagen hydrogel for cardiac cell culture and delivery *Acta Biomater.* **8** 1022–36
- [74] Kitsigianis G A, O'Leary D P and Davis L L 1988 Active head-movement analysis of cisplatin-induced vestibulotoxicity *Otolaryngol. Head Neck Surg.* **98** 82–87
- [75] Bonewald L F and Johnson M L 2008 Osteocytes, mechanosensing and Wnt signaling *Bone* **42** 606–15
- [76] Liegibel U M, Sommer U, Bundschuh B, Schweizer B, Hilscher U, Lieder A, Nawroth P and Kasperk C 2004 Fluid shear of low magnitude increases growth and expression of TGFbeta1 and adhesion molecules in human bone cells *in vitro Exp. Clin. Endocrinol. Diabetes* **112** 356–63
- [77] Nicoletta D P, Moravits D E, Gale A M, Bonewald L F and Lankford J 2006 Osteocyte lacunae tissue strain in cortical bone *J. Biomech.* **39** 1735–43
- [78] Batra N, Kar R and Jiang J X 2012 Gap junctions and hemichannels in signal transmission, function and development of bone *Biochim. Biophys. Acta* **1818** 1909–18
- [79] Li X, Liu C, Li P, Li S, Zhao Z, Chen Y, Huo B and Zhang D 2013 Connexin 43 is a potential regulator in fluid shear stress-induced signal transduction in osteocytes *J. Orthop. Res.* **31** 1959–65
- [80] Qin L, Liu W, Cao H and Xiao G 2020 Molecular mechanosensors in osteocytes *Bone Res.* **8** 23
- [81] Geoghegan I P, Hoey D A and McNamara L M 2019 Integrins in osteocyte biology and mechanotransduction *Curr. Osteoporos. Rep.* **17** 195–206
- [82] Murugan R and Ramakrishna S 2005 Development of nanocomposites for bone grafting *Compos. Sci. Technol.* **65** 2385–406
- [83] Wang W and Yeung K W K 2017 Bone grafts and biomaterials substitutes for bone defect repair: a review *Bioact. Mater.* **2** 224–47
- [84] Jeong J, Kim J H, Shim J H, Hwang N S and Heo C Y 2019 Bioactive calcium phosphate materials and applications in bone regeneration *Biomater. Res.* **23** 4
- [85] Ogose A, Kondo N, Umezue H, Hotta T, Kawashima H, Tokunaga K, Ito T, Kudo N, Hoshino M and Gu W 2006 Histological assessment in grafts of highly purified beta-tricalcium phosphate (OSferion) in human bones *Biomaterials* **27** 1542–9
- [86] Ielo I, Calabrese G, De Luca G and Conoci S 2022 Recent advances in hydroxyapatite-based bio-composites for bone tissue regeneration in orthopedics *Int. J. Mol. Sci.* **23** 9721
- [87] Okada S, Ito H, Nagai A, Komotori J and Imai H 2010 Adhesion of osteoblast-like cells on nanostructured hydroxyapatite *Acta Biomater.* **6** 591–7
- [88] Overgaard S, Lind M, Josephsen K, Maunsbach A B, Bunger C and Soballe K 1998 Resorption of hydroxyapatite and fluorapatite ceramic coatings on weight-bearing implants: a quantitative and morphological study in dogs *J. Biomed. Mater. Res.* **39** 141–52
- [89] Xu Z, Liu C, Wei J and Sun J 2012 Effects of four types of hydroxyapatite nanoparticles with different nanocrystal morphologies and sizes on apoptosis in rat osteoblasts *J. Appl. Toxicol.* **32** 429–35
- [90] Kanis J A 1996 Estrogens, the menopause, and osteoporosis *Bone* **19** 185S–90S
- [91] McNamara L M 2021 Osteocytes and estrogen deficiency *Curr. Osteoporos. Rep.* **19** 592–603
- [92] Gong H et al 2008 Glucocorticoids antagonize estrogens by glucocorticoid receptor-mediated activation of estrogen sulfotransferase *Cancer Res.* **68** 7386–93